ALMA Observations of the Spatial Distribution of three C<sub>2</sub>H<sub>4</sub>O<sub>2</sub> Isomers towards Sgr B2(N)

CI XUE, ANTHONY J. REMIJAN, ANDREW M. BURKHARDT, 3, 4 AND ERIC HERBST 1, 3

 $^1Department\ of\ Chemistry,\ University\ of\ Virginia,\ Charlottes ville,\ VA\ 22904,\ U.S.A$ 

<sup>2</sup>National Radio Astronomy Observatory, Charlottesville, VA 22903, U.S.A

<sup>3</sup>Department of Astronomy, University of Virginia, Charlottesville, VA 22904, U.S.A

<sup>4</sup>Harvard-Smithsonian Center for Astrophysics, Cambridge, MA 02138, U.S.A

(Received September 14, 2018; Revised November 26, 2018; Accepted December 7, 2018)

# Submitted to ApJ

# ABSTRACT

The  $C_2H_4O_2$  isomers have been previously investigated primarily via disparate sets of observations involving single dish and array measurements. The only attempt at using a uniform set of observations was performed with the IRAM 30 m observation in 2013 (Belloche et al. 2013). In this study, we present an intensive and rigorous spectral and morphological analysis of the  $C_2H_4O_2$  isomers towards Sgr B2(N) with interferometers, ALMA Band 3 observations. We propose a quantitative selection method, which automates the determination of the most uncontaminated transitions and allows us to report the discovery of previously undetected transitions of the three isomers. With the least contaminated transitions, the high spatial-resolution millimeter (mm) maps of the  $C_2H_4O_2$  isomers reveal that HCOOCH<sub>3</sub> and  $CH_2OHCHO$  each display two different velocity components, while only one velocity component of  $CH_3COOH$  is resolved.

Corresponding author: CI XUE

cx5up@virginia.edu

Moreover, the distribution of HCOOCH<sub>3</sub> is extended and offset from the continuum emission, unlike CH<sub>2</sub>OHCHO and CH<sub>3</sub>COOH, for which the low-velocity component is found to be compact and concentrated toward the continuum emission peak of Sgr B2(N). The distinct morphologies of these C<sub>2</sub>H<sub>4</sub>O<sub>2</sub> isomeric species indicate that HCOOCH<sub>3</sub> have significant differences in chemical processes than CH<sub>2</sub>OHCHO and CH<sub>3</sub>COOH, which display similar spatial distributions.

Keywords: astrochemistry — line: identification — ISM:individual(Sagittarius B2)—
ISM:molecules

### 1. INTRODUCTION

Isomers are families of molecules that share the same constituent atoms, but are uniquely arranged and, as such, have very different chemical properties. Several isomeric groups are well known to exist in the interstellar medium (ISM). Examples include HCN and HNC towards translucent clouds (Turner 1991) and proroplanetary disks (Graninger et al. 2015), as well as CH<sub>3</sub>CN and CH<sub>3</sub>NC (Remijan et al. 2005) and three isomers of C<sub>3</sub>H<sub>2</sub>O (Loomis et al. 2015) toward Sagittarius B2 North (Sgr B2(N)). Because isomers have different chemical and physical properties, further insight can be gained into the astrochemical evolution of different physical environments of astronomical sources by making use of isomers.

One way this can be accomplished is with the Minimum Energy Principle (Lattelais et al. 2009, 2010, 2011). However, it has already been refuted with numerous examples of isomers (Belloche et al. 2014; Karton & Talbi 2014). Instead, it is widely accepted that the relative abundance of structural isomers in the ISM depends more on their formation mechanisms, i.e. kinetically controlled, than their relative energy differences, assuming they have same destruction routes, which has been further supported by Loomis et al. (2015). Thus, the study of isomers can help to constrain temperature-and density-dependent synthetic routes to complex interstellar molecules (Mottl et al. 2007), which may in turn help to explain spatial distributions.

This work focuses on three isomers of C<sub>2</sub>H<sub>4</sub>O<sub>2</sub>: glycolaldehyde (CH<sub>2</sub>OHCHO, GLA), acetic acid (CH<sub>3</sub>COOH, AcA) and methyl formate (HCOOCH<sub>3</sub>, MF), the chemical evolution of which has been widely investigated (Laas et al. 2011; Skouteris et al. 2018; Linnartz et al. 2015). In astrochemical models, the most widely used mechanism to efficiently form the C<sub>2</sub>H<sub>4</sub>O<sub>2</sub> isomeric family in hot cores is through radical-radical recombination on interstellar grain surfaces (Garrod et al. 2008; Chuang et al. 2016). However, in addition to grain surface chemistry, it was also suggested that MF could be formed via gas-phase processes in cold regions (Laas et al. 2011; Balucani et al. 2015). An understanding of the astrochemical evolution of the C<sub>2</sub>H<sub>4</sub>O<sub>2</sub> isomers can shed light on calibrating astrochemical modeling networks. Furthermore, there has been increasing interest in studying these isomers towards astronomical environments because of their importance in the formation of large biologically-relevant molecules (Wächtershaüser 2000; Liu et al. 2001, 2002; Puletti et al. 2010).

The northern clump of Sgr B2(N) molecular cloud, which lies ~120 pc from the Galactic center, is one of the most massive star-forming regions in the Galaxy. In 2011, observations with the SMA at a spatial resolution of 0."4 × 0."24 revealed two emission cores within the millimeter continuum map of Sgr B2(N) (Qin et al. 2011). One of these located at  $\alpha_{J200} = 17h47m19.889s$ ,  $\delta_{J2000} = -28^{\circ}22'18.22''$  was designated as N1 in Belloche et al. (2016) and the other located at  $\alpha_{J2000} = 17h47m19.885s$ ,  $\delta_{J2000} = -28^{\circ}22'13.29''$  was designated as N2 in Belloche et al. (2016). The prominent core, N1, which contains the well known Sgr B2(N) Large Molecule Heimat (LMH) source (Snyder, Kuan & Miao 1994), is located ~ 5" south of N2. The two cores have different systematic velocities,  $V_{\rm lsr}$ , ~ 64 km s<sup>-1</sup> for N1 and ~ 73 km s<sup>-1</sup> for N2 (Belloche et al. 2013). Recently, the hot core structures in Sgr B2(N) was further characterized and up to 20 continuum sources were reported (Bonfand et al. 2017; Sánchez-Monge et al. 2017). Here, we adopt the naming conventions LMH and the shorthand notation of the continuum emission cores of N1, N2 and N3. The coordinates of N3 is  $\alpha_{J2000} = 17h47m19.248s$ ,  $\delta_{J2000} = -28^{\circ}22'14.91''$  as described in Bonfand et al. (2017). See Section 4 for the corresponding positions.

Sgr B2(N) is one of the most prolific regions for detecting Large Astronomical Molecules (LAMs). Here, we move away from Complex Organic Molecules (COMs) (Herbst & van Dishoeck 2009) and use

LAMs as a more accurate definition for astronomical molecules with more than 6 atoms on account of the fact that, in astronomical environment, many detected molecules are not complex by chemical standards and have no direct relationship to organic or prebiotic chemistry. Many LAMs were first detected toward this source, such as CH<sub>2</sub>CHCHO and CH<sub>3</sub>CH<sub>2</sub>CHO (Hollis et al. 2004), NH<sub>2</sub>CH<sub>2</sub>CN (Belloche et al. 2008), CH<sub>3</sub>NCO (Halfen et al. 2015) and CH<sub>3</sub>CHCH<sub>2</sub>O (McGuire et al. 2016). The first detection of all of the three C<sub>2</sub>H<sub>4</sub>O<sub>2</sub> isomers were also reported towards Sgr B2. The discovery of MF was achieved with the Parkes 64 m telescope in 1975 (Brown et al. 1975), while the lower abundance isomers, AcA and GLA, were not detected until several decades later due to the lack of accurate laboratory data. Mehringer et al. (1997) reported the first detection of 4 strong transitions of AcA towards the LMH region in Sgr B2(N) using the Berkeley Illinois Maryland Association (BIMA) Array and the Caltech Owens Valley Radio Observatory (OVRO) millimeter array, while the first detection of GLA was not reported until Hollis et al. (2000) who used the NRAO 12m telescope.

The C<sub>2</sub>H<sub>4</sub>O<sub>2</sub> isomers have been previously investigated primarily via disparate sets of observations involving single dish and array measurements. The MF and GLA abundance ratio, [HCOOCH<sub>3</sub>]:[CH<sub>2</sub>OHCHO], toward Sgr B2(N) was reported to be  $\sim 6.7:1$  as observed with the NRAO 12 m single-dish telescope (Hollis et al. 2000). Hollis et al. (2001) further studied MF and GLA with the BIMA array and found the abundance ratio to be  $\sim 52:1$  for [HCOOCH<sub>3</sub>]:[CH<sub>2</sub>OHCHO]. The difference between the ratios was interpreted to be due to the different beam sizes between the single dish and interferometric array observations and to the size of the source of the molecular emission towards the LMH region. The one attempt at using a uniform set of observations was performed with the IRAM 30 m (Belloche et al. 2013). They deduced the abundance ratios among the three molecules [HCOOCH3]: [CH2OHCHO]: [CH3COOH] to be 242:1:5.8 with unconstrained temperatures and source sizes. Regarding the spatial distributions, although Hollis et al. (2001) mapped both MF and GLA with the BIMA array, the images were only based on a single transition of GLA, 8(0,8) - 7(1,7), and the blended transitions of MF: 7(5,3) - 6(5,2) E and 7(5,2) - 6(5,1) A. The extended and cool distribution of GLA suggested with the BIMA array observations indicated a gas phase formation mechanism. MF is ubiquitous in molecular cores with various physical conditions,

suggesting that its formation involves both gas-phase and grain-surface processes. AcA always possesses a warm, compact distribution, which favors grain surface formation mechanisms (Mehringer et al. 1997) followed presumably by thermal desorption.

Therefore, a rigorous comparison between the abundances and overall spatial distributions of these three isomers has not been achieved. High-sensitivity observations with better spatial and spectral resolution are necessary to determine accurate abundance ratios and molecular morphology in different regions towards Sgr B2(N). As such, a new careful comparison of these triplets towards the Sgr B2(N) region is needed. The Atacama Large Millimeter/submillimeter Array (ALMA) has the ability to carry out observations of molecules with low abundances and weak emission lines and to image LAMs at small spatial scales due to its high sensitivity and angular resolution (Öberg et al. 2015).

This work reports a self-consistent and rigorous investigation of three  $C_2H_4O_2$  isomeric species with interferometric observations towards Sgr B2(N). The observations are summarized in Section 2. Section 3 describes the methods and results of the data analysis, including the selection processes for selecting the unblended transitions of each species. The spatial distributions of  $C_2H_4O_2$  isomers are presented in detail in Section 4. The possible explanations for the difference of the spatial distribution of each molecular species is discussed in Section 5, and the conclusion is given in Section 6.

### 2. OBSERVATIONS

The interferometric data used here were acquired from the ALMA Science Archive<sup>1</sup> of the EMoCA survey (Exploring Molecular Complexity with ALMA) (Belloche et al. 2016). This survey included 5 spectral setups as shown in Table 1 of which S1-S4 were performed during Cycle 0 (2012) with ALMA project code 2011.0.00017.S and S5 during Cycle 1 (2014) with project code 2012.1.00012.S. Each setup contains 4 spectral windows within the overall frequency range from 84.1 to 114.4 GHz. The phase center of the observations was pointed toward Sgr B2 with the field center at  $\alpha_{J2000} = 17h47m19.87s$ ,  $\delta_{J2000} = -28^{\circ}22'16''$ . The Half Power Beam Width (HPBW) of the primary beam

<sup>1</sup> http://almascience.nrao.edu/aq/

measured from actual 12 m ALMA antennas was 69" and 51" at 84 and 114 GHz respectively (Remijan et al. 2015). The spectral resolution was 488.3 kHz, which corresponds to a velocity resolution of 1.29 to 1.70 km s<sup>-1</sup> across the observing band. A detailed description of the observations and the data calibration was presented in Belloche et al. (2016).

The Common Astronomy Software Applications package (CASA) (McMullin et al. 2007) was used for imaging and analysis. For each spectral window, the relatively line-free continuum channel ranges were selected with the techniques, as described in McGuire et al. (2017), which are based on the mean spectrum generated from the CASA image cube. Afterwards, the ranges were used to subtract the continuum emission in the UV-plane before imaging the spectral cubes. The imaging parameters of each spectral window are presented in Table 1. For all data sets, we used the Briggs scheme with a robust parameter of 0.5 and a cell size of 0.3" for imaging. The resulting size of the synthesized beam (HPBW) of each data cube has a medium value  $\sim 1.6$ ". The median of resultant typical rms noise levels is 4.4 mJy beam<sup>-1</sup>.

## 3. SPECTRAL ANALYSIS

#### 3.1. Transition Selection Processes

Although MF, GLA and AcA have been unambiguously detected toward Sgr B2, the identification of clear individual spectral features of GLA and AcA were not obvious because of the spectral confusion, which limited the number of uncontaminated lines. Here, we propose a more reliable way to uniquely identify the spectral features of the C<sub>2</sub>H<sub>4</sub>O<sub>2</sub> isomers towards Sgr B2(N), particularly the spectral features of AcA and GLA. Through a more accurate continuum subtraction and our methods of line identification, we identified weaker, and previously undetected, transitions of this isomeric triplet from the EMoCA survey (Belloche et al. 2016) and further selected the least contaminated transitions for imaging.

Snyder et al. (2005) proposed five criteria, hereafter referred to as the Snyder Criteria, for line assignments, particularly toward interstellar clouds with high spectral line densities greater than 10 lines per 100 MHz, see also (Calcutt et al. 2014; Remijan et al. 2014; Brouillet et al. 2015;

Table 1. Summary of Analyzing Parameters

Setup	SPW	Frequency Range	Primary Beam	Synthesized	Beam <sup>a</sup>	Spectral	Median rms <sup>b</sup>
			HPBW	HPBW	PA	Resolution	Per Channel
		$\mathrm{GHz}$	"	"×"	0	$\rm km\ s^{-1}$	${ m mJy~beam^{-1}}$
S1	0	84.091 - 85.966	69	$2.14 \times 1.56$	-85.5	1.70	4.1
	1	85.904 - 87.779	67	$2.06\times1.54$	-84.4	1.69	3.5
	2	96.154 - 98.029	60	$1.85\times1.41$	-87.2	1.51	3.5
	3	97.904 - 99.779	59	$1.81\times1.39$	-86.7	1.48	3.8
S2	0	87.729 - 89.604	66	$3.00\times1.36$	-82.8	1.65	4.5
	1	89.554 - 91.429	64	$2.96\times1.36$	-83.4	1.62	4.5
	2	99.728 - 101.602	58	$2.68 \times 1.21$	-83.7	1.46	4.4
	3	101.552 - 103.427	57	$2.58\times1.21$	84.4	1.43	4.6
S3	0	91.368 - 93.242	63	$3.01\times1.47$	84.8	1.59	5.7
	1	93.193 - 95.067	62	$2.94\times1.48$	84.7	1.56	5.6
	2	103.365 - 105.239	56	$2.68 \times 1.32$	85.1	1.40	6.8
	3	105.189 - 107.064	55	$2.59\times1.31$	83.9	1.38	7.1
S4	0	95.021 - 96.896	61	$1.82\times1.40$	-83.1	1.53	4.0
	1	96.846 - 98.720	60	$1.80\times1.38$	-82.1	1.50	3.1
	2	107.019 - 108.893	54	$1.62\times1.24$	-84.0	1.36	3.8
	3	108.843 - 110.718	53	$1.58\times1.22$	-82.3	1.33	3.8
S5	0	98.672 - 100.546	58	$1.79\times1.46$	-74.2	1.47	3.2
	1	100.496 - 102.370	57	$1.76\times1.43$	-73.7	1.44	5.0
	2	110.669 - 112.543	52	$1.61\times1.30$	-75.6	1.31	5.7
	3	112.494 - 114.368	51	$1.56\times1.29$	-73.4	1.29	5.6

**Note**—

aThe synthesized beam size varies depending on the robust parameter. Here we used a robust parameter of 0.5.

 $<sup>^{</sup>b}$ The estimated rms noise level of each spectral window is the median of the noise levels measured in several channels with moderate emission, where the noise levels are each measured in the off-source region.

Carroll et al. 2015). The Snyder Criteria, which are utilized in our study, include: (i) accurate rest frequencies, (ii) beam dilution, (iii) frequency agreement, (iv) line intensity and (v) presence of transitions with observable intensity. Here we applied these criteria for identifying the mostly uncontaminated transitions of the  $C_2H_4O_2$  isomers. In the following, we discuss each criterion of the Snyder Criteria with our line identification process for the  $C_2H_4O_2$  isomers. Details about other applications and the scope of the criteria are presented in Snyder et al. (2005).

(i) Accurate Rest Frequencies. The first criterion is the need for high degree of accuracy of the rest frequency of the target molecular transitions. The millimeter wave spectrum of GLA has been studied in the laboratory by Butler et al. (2001), Widicus Weaver et al. (2005), and Carroll et al. (2010); the spectrum of MF by Oesterling et al. (1999), Ogata et al. (2004), and Carvajal et al. (2007), and the spectrum of AcA by Ilyushin et al. (2001, 2013). Their transitions are included in the current public databases: the CDMS catalog <sup>2</sup> (Müller et al. 2005), the JPL catalog <sup>3</sup> (Pickett et al. 1998) and the Spectral Line Atlas of Interstellar Molecules (SLAIM) database, which are available in the SPLATALOGUE spectroscopy database <sup>4</sup>. For the analysis of the present ALMA observations, the rest frequencies and other spectral line parameters of the three isomers were taken from the above databases. In the range of 84-114 GHz, the transition uncertainties of the three molecules were estimated to be less than 150 kHz, compared to a spectral resolution of 488.3 kHz. As a result, our study satisfied the criteria of the high accuracy in rest frequency.

In this study, we consider the transitions for both the ground and first vibrationally excited states of MF but only the vibrational ground state of AcA and GLA. The high hot cores temperatures ( $\sim 150\text{-}200 \text{ K}$ , Belloche et al. (2016)) along with the high abundance of interstellar MF make the low-energy vibrationally excited states of MF ( $v_t = 1$  at  $\sim 132 \text{cm}^{-1}$  or 190 K) likely to be populated in hot cores (Sakai et al. 2015). In fact, transitions within  $v_t = 1$  of

<sup>&</sup>lt;sup>2</sup> https://www.astro.uni-koeln.de/cdms/catalog

<sup>&</sup>lt;sup>3</sup> https://spec.jpl.nasa.gov

<sup>4</sup> https://www.splatalogue.net

MF have been reported toward Orion KL (Kobayashi et al. 2007) and W51 e2 (Demyk et al. 2008), which are comparable hot cores to Sgr B2. Belloche et al. (2016) derived the rotational temperatures in Sgr B2(N) ranging from 112-278 K for different LAMs. Considering the excitation temperature and the previously determined column density of  $N_{\rm HCOOCH_3} \sim 1.2 \times 10^{18} {\rm cm}^{-2}$  (Belloche et al. 2016), both the ground and  $v_{\rm t}=1$  states are studied in this work. Even though the comparable first vibrationally excited state of AcA lies at about 170 cm<sup>-1</sup> (or 245 K) above the ground state (Ilyushin et al. 2001) and that of GLA at 195 cm<sup>-1</sup> (or 280 K) (Widicus Weaver et al. 2005), their abundances are not high enough to be detectable toward Sgr B2(N) like MF (Hollis et al. 2001; Remijan et al. 2002). Therefore, only the vibrational ground states for AcA and GLA are considered in this study.

(ii) Beam Dilution. The correction based on the beam dilution effects arises from the different synthesized beam sizes of the telescopes, which affect the relative intensities measured for spectral lines toward the same pointing position. Therefore, the relative observed intensities between any transitions need to be corrected for beam dilution effects when the observations are carried out with different telescopes (Remijan et al. 2014). In this study, the observations were carried out in the same receiver band, ALMA Band 3. The minimum size of the synthesized beam of the EMoCA survey was reported as 1.58" × 1.22" while the source diameters, the FWHM from two-dimentional Gaussian fits to the integrated intensity maps, of many LAMs, including MF, were reported to be not larger than 1.5" (Belloche et al. 2016). Therefore beam dilution should not affect the corresponding line intensity difference of the three isomers if they have similar source sizes. In fact, we find that the three isomers have different source sizes as shown in Section 4. But, given the measurement accuracy and the resolution of the EMoCA survey, the angular extent of all emission above 3 σ for the three isomers is larger than the synthesized beam of the observations. The beam dilution effect in our analysis is thus negligible.

To examine whether our line assignments satisfy the other three Snyder criteria, we applied a single-excitation temperature simulation followed with a quantitative analysis approach, which automatically reduces the number of emission line candidates by filtering out the obviously blended lines. The remaining less blended transitions go through a more rigorous analysis including spatial distribution imaging.

In this study, the observed spectra presented are extracted from the largest synthesized beam with a size of 3.01"  $\times$  1.47" centered at LMH with the centroid position at  $\alpha_{\rm J200}=17\rm h47m19.930s$ ,  $\delta_{\rm J2000}=-28^{\circ}22'18.200''$ . The LMH region is dense with  $n_{\rm H_2}({\rm Sgr~B2(N)})>10^9~{\rm cm}^{-3}$  (Sánchez-Monge et al. 2017), and hence LTE is assumed to be reached. Although there is still some likelihood of non-thermal excitation, the molecular emission toward LMH should be well-described by spectra simulated with a single-excitation temperature ( $T_{\rm ex}$ ) (McGuire et al. 2017). The single-excitation model follows the convention of Hollis et al. (2004) with corrections for optical depth as discussed in Turner (1991) and Mangum & Shirley (2015). The spectra are simulated from the catalog data available in the public databases, which were generated from the laboratory data.

By comparing the simulated spectra with the observed spectra, we fit the observed spectrum of each molecule to constrain (1) the spectral line width  $(\Delta V)$ , (2) the source velocity  $(V_{\rm lsr})$ , (3) the molecular column density  $(N_T)$ , and (4) the excitation temperature  $(T_{\rm ex})$  which contributes to the relative intensities among transitions of a certain species.

To determine the best fit to the observed spectrum, a variety of simulations with different values of these key quantities was constructed. We left both  $N_T$  and  $T_{\rm ex}$  as free parameters to be adjusted and tried to obtain the best-fit simulation. By setting the  $\Delta V$  to 6.5 km s<sup>-1</sup>,  $V_{\rm lsr}$  to 64 km s<sup>-1</sup>,  $T_{\rm ex}$  to 190 K, we find that though subjective the single-excitation temperature simulations yield the most consistent fit to the observed spectra. The  $V_{\rm lsr}$  and  $\Delta V$  toward LMH were constrained by previous studies to the values of 64 km s<sup>-1</sup> for  $V_{\rm lsr}$  and  $\sim$  7 km s<sup>-1</sup> for  $\Delta V$  (Belloche et al. 2008). The parameter  $T_{\rm ex}$  used here is consistent with the value of 200 K for  $T_{\rm rot}$  used in Mehringer et al. (1997) for AcA and MF. It should be noted that these spectra are used for the initial analysis for identifying

the potential uncontaminated transitions only and the values of  $N_T$  and  $T_{\rm ex}$  will be refined later by  $\chi^2$  fitting using only the uncontaminated transitions as discussed in Section 3.3.

In order to quantify the degree of consistency between the simulated and observed spectra, we further defined two factors to describe this degree of consistency of line profiles, which quantify two of the Snyder Criteria: (iii) frequency and (iv) line intensity agreement.

The spectral range for comparing line profiles from observation and simulation is crucial for calculating these consistency factors. As illustrated in Figure 1, within the small spectral range shown in blue, the simulated line shows a high degree of agreement in line intensity with the observed line. As a matter of fact there are two observed lines blended with each other. But, if a larger spectral range is used for comparing, the blended part colored in orange would be taken into account and thus reduce the degree of consistency. Therefore, using a large spectral range yields a value that describes the situation more accurately. In addition, as required by the Snyder criterion for frequency agreement, a resolved transition should be separated from its adjacent lines by more than its FWHM. So the spectral range for comparing line profiles should at least include the contiguous channels of which the simulated intensities are larger than 50% of the peak intensity. As it is critical to have a clean transition for imaging, in our study, we adopt an even wider spectral range where only the channels with intensities larger than 10% of the maximum are considered.

(iii) Frequency agreement. For characterizing the proximity in central frequencies, we define the P (Product) factor, which is based on the product of the observed and simulated line profiles, in the following manner:

$$P \text{ factor} = \frac{\sum_{\nu_1}^{\nu_2} I_{\text{obs}} \times I_{\text{sim}}}{\sum_{\nu_1}^{\nu_2} I_{\text{obs}}^{\text{sorted}} \times I_{\text{sim}}^{\text{sorted}}}$$
(1)

In Equation (1),  $I_{\text{obs}}$  and  $I_{\text{sim}}$  are the observed and simulated intensity as functions of frequency respectively. Figure 2(a) shows a fictitious simulated spectrum in red and a fictitious observed spectrum in black. The product of the profiles in each channel is first calculated and plotted in Figure 2(b). For example, in Figure 2(a), the observed value in channel 10 is 0.835 and the simulated value is 0.643. Therefore, the product is 0.537 as shown in channel 10 of Figure 2(b).

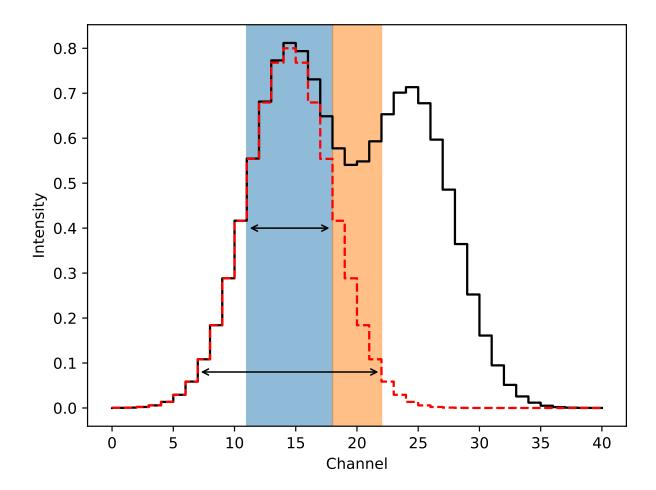


**Figure 1.** Illustration of the effect of different spectral range for comparing line profiles. Simulated spectrum and observed spectrum are shown in red dashed line and black solid line respectively.

The simulated and observed spectrum are then sorted in intensity bins from lowest intensity (left) to highest intensity (right) in Figure 2(c) and denoted by  $I_{\text{sim}}^{\text{sorted}}$  and  $I_{\text{obs}}^{\text{sorted}}$  respectively. Once again, similar to Figure 2(b), we derived the product of the sorted spectra for each bin as shown in Figure 2(d). Finally, the P factor is calculated by dividing the area in Figure 2(b) by the area in Figure 2(d). The denominator represents the maximum achievable value of the numerator and normalizes the P factor to 100%. In this example, since the central frequencies of the spectra are inconsistent, we obtain a rather low P factor, 82%.

If the central frequencies of the compared lines are same, the bin of the simulated and observed intensity in each channel would be the same. So, after sorting, only the order would change but the product of intensity would remain the same. The P factor thus would reach 100%. Figure 3 shows a couple of examples of the spectra with corresponding 5%, 25%, 50% and 100% P-values.

In our analysis, the summation operations in Equation (1) sum over the spectral range in which the simulated intensities larger than 10% of its maximum as mentioned above. The threshold P factor for assigning a line depends on the situation. In the study of  $C_2H_4O_2$  toward Sgr B2(N), we have a high confidence of the accuracy of rest frequencies for the three molecules and the source velocity of LMH, which are the major factors affecting the frequency agreement. As a result, we are rigorous with the P factor and assign a transition with a P factor at least larger than 90% to be an unblended transition candidate.

(iv) Line Intensity. The difference of the line intensities is measured by the D (Difference) factor.
It is the ratio between the difference of the integrated intensities of the compared spectra and the maximum of the two subtracted from 1:

$$D \text{ factor} = 1 - \frac{\left| \sum_{\nu_1}^{\nu_2} I_{\text{obs}} - \sum_{\nu_1}^{\nu_2} I_{\text{sim}} \right|}{\max\left( \sum_{\nu_1}^{\nu_2} I_{\text{obs}}, \sum_{\nu_1}^{\nu_2} I_{\text{sim}} \right)}$$
(2)

Similar to Equation (1), in Equation (2),  $I_{\text{obs}}$  and  $I_{\text{sim}}$  are the observed and simulated intensity, respectively, and the D factor is calculated using the same spectral range of the P factor. Figure 4 shows fictitious observed and simulated lines with different intensities. The hashed area in Figure 4(a), which represents the numerator in Equation (2), is the difference in integrated line intensities while the filled area in Figure 4(b), which represents the denominator is the maximum of the two integrated intensities. In this example, the D factor is 39%.

When there is no difference in the intensities, the numerator is 0. As a result, the D factor is normalized to 100%. In the worst case, where there is no emission in one of the spectra, the numerator would be same as the denominator and the D factor equals 0%. Figure 5 shows a couple examples of the spectra with a 5%, 25%, 50% and 100% D-value correspondingly.

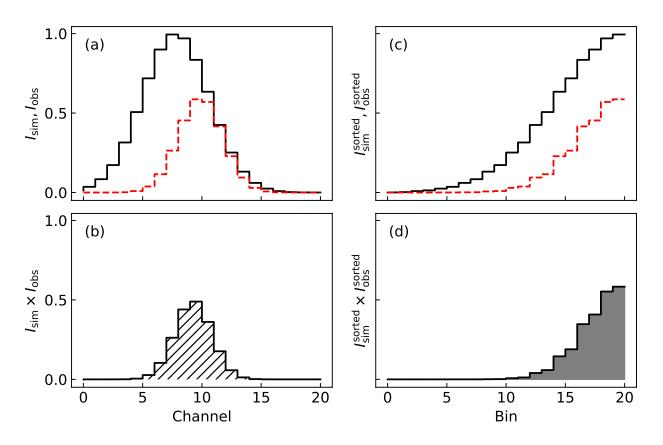


Figure 2. Illustration of the calculation of the P factor. In panel (a), the black solid lines represent the fictitious observed data while the red dashed lines represent the fictitious simulated data. Panel (b) represents the product of the compared spectra, i.e. the numerator in equation (1). Panel (c) shows the spectra sorted in their intensities. The products of the sorted spectra are plotted in panel (d) of which the areas represents the denominator in Eq. (1). The P factor is 82% in this case.

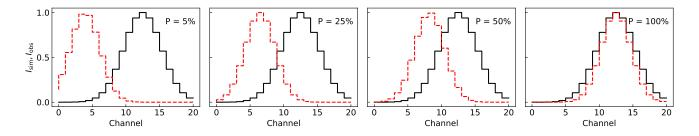


Figure 3. Examples of the compared spectra with P factors of 5%, 25%, 50% and 100% which are plotted in solid and dashed lines respectively.

The threshold of the D factor depends on the accuracy of the input temperature, line width and column density for simulating spectra to the actual values. However, there are still uncertainties in these input parameters, so that a relatively high tolerance of the difference of line intensities between the simulated and observed spectrum is needed. To decide the threshold of the D factor, many simulations were run over a wide range of temperature and column density, with significant deviation in line intensity occurring when the D factor dropped below 60%. Therefore, in this study, we set a threshold of 60% for the D factor.

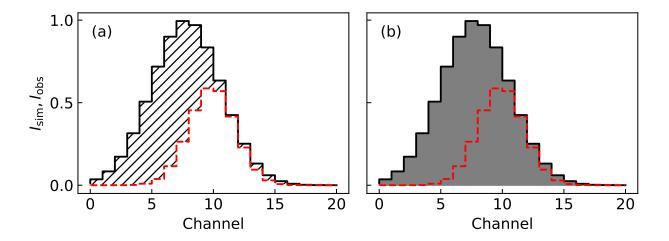


Figure 4. Illustration of the calculation of the D factor. The fictitious compared spectra are plotted in solid and dashed lines respectively. The hatched area in panel (a) represents the numerator in equation (2) while the filled area in panel (b) represents the denominator. The D factor is 39% in this case.

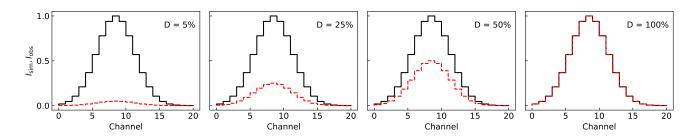


Figure 5. Examples of the compared spectra with D factors of 5%, 25%, 50% and 100% which are plotted in solid and dashed lines respectively. The compared spectra are given the same central frequencies.

(v) Presence of Transitions with Observable Intensity. The fifth and last Snyder criterion suggests that all transitions with intensity predictions leading to detectable signal levels must be present. We further confirmed the candidate transitions by checking their corresponding connected transitions, i.e. the transitions connected by favorable transition probabilities (Snyder et al. 2005). Similarly to the connected transitions, the A-E pair transitions for MF and AcA have similar line strengths, energy levels, and transition probabilities, and therefore each pair of transitions should have roughly the same intensity and line shape. Both the A and E state transitions must be detected if any of them has a detectable signal level. In this work, all the transitions of the three isomers with observable intensities are present and none of the strong lines is missing within the observed spectra, although a large number of these lines are blended with neighboring features which leads to small P and D factors for these lines.

We are aware that our selection method suffers from several limitations: (1) There is the possibility of having absorption in the observed spectra. In that case, the methods of making use of the above consistency factors will be broken and the resulting factors would have abnormal values such as values larger than 100% or negative values. Therefore, we exclude the transitions when there is obvious absorption into our calculations of P and D values. (2) The transition maps of unblended transitions might suffer from the contamination of spatial distributions, which could not be recognized by analyzing the spectrum toward one region. To avoid this problem, we have additionally checked every interferometric transition map of the less contaminated transitions found by our methods and marked the spatially polluted transitions, as discussed in Section 4.1. (3) Unfortunately, due to the large line width and the high density of emission lines at mm wavelengths, lines could be blended very frequently with adjacent emission lines of the same molecule and appear as single-line spectral features. These transitions still have high values of P and D and would be identified as clean transitions. However, since their line profiles overlap with one another, they do not qualify for imaging. Thus, we carefully inspect the spectra of the transitions with the two consistency factors over our thresholds and highlight these kinds of "grouped" transitions, as discussed in Section 3.2-

HCOOCH<sub>3</sub>. These limitations reveal the complexity and difficulty of identifying and mapping a molecule in a source with high spectral line densities.

In spite of its shortcomings, as the focus of the study is on the rotational emission transitions of the  $C_2H_4O_2$  isomers, the transition selection processes in this study is in accordance with the rigorous Snyder criteria. This method also facilitated the detection of weaker and undiscovered transitions of our targets and enabled automation of the analysis of a survey with a large bandwidth by quantifying the consistency of the observed and simulated spectra. The details of the transition selection for the three isomers are summarized below.

# 3.2. Transitions of $C_2H_4O_2$

For assigning the least contaminated transitions, we set thresholds for both P and D factors respectively to select the corresponding transition candidates first. Theoretically, the two factors for a clean transition, which has no difference in either center frequency or line intensity between observed and simulated lines, are both 100%. In this study, we assign a transition with a P factor at least larger than 90% and a D factor larger than 60% to be an unblended transition candidate. After that, we further check if there is serious contamination from other transitions of the same molecule and if the spatial distribution is consistent with other transitions. The details of the selection of the most uncontaminated transitions of MF, GLA and AcA are now detailed.

 $HCOOCH_3$ —Within the observed spectral range, 84091 to 114368 MHz, there are 1516 transitions of MF recorded in the JPL catalog, including both the vibrationally ground state and first torsionally excited state. In the LTE simulated spectra of MF with an excitation temperature of  $T_{\rm ex} = 190 \, \text{K}$ , 197 transitions were found to be above a signal-to-noise (S/N) level of 3 and are potentially detectable.

Through calculating the correlation factors, there are 26 MF transitions, which have P factors larger than 95% and D factors larger than 60% and satisfy our criteria. These 26 transitions of MF are shown in Figure 6 and given in Table 2 with the following parameters: rest frequency(uncertainty) in MHz, rotational quantum number, upper-state energy  $(E_u)$  in Kelvin, intensities expressed as the product of the relevant component of the dipole moment squared times transition strength  $(S_{ij}\mu^2)$ 

in Debye<sup>2</sup> (Townes & Schawlow 1975), FWHM in MHz, critical density  $(n_{\text{crit}})$  in  $cm^{-3}$  and the two resulting correlation factors.

Many of A-E pairs and connected transitions of MF usually have little difference in frequencies compared to the observed line width, some of which are almost completely blended with each other and appear as a single line spectral feature. Therefore, as mentioned before, the strict use of our methodology for comparing spectral lines fails to identify these wide spectral features. As expected, there are several sets of transitions blended together among the 26 MF transitions. Therefore, we only imaged the transition maps of the remaining 10 transitions of MF which are the least contaminated, including 2 transitions in the  $v_t = 1$  state, 9(1,8) - 8(1,7) A v = 1 and 8(3,5) - 7(3,4) A v = 1.

MF has been widely studied in the ISM. Previous studies that targeted Sgr B2(N) reported several transitions of MF, within the frequency coverage of the EMoCA survey (Hollis et al. 2001; Remijan et al. 2002, 2003; Requena-Torres et al. 2006). We critically examined seven transitions of MF from Hollis et al. (2001), two from Remijan et al. (2002), six from Remijan et al. (2003), and seven from Requena-Torres et al. (2006), and found that most of these previously reported transitions are contaminated by adjacent lines in the observed spectra toward LMH and have relatively low P and P values. Only the 7(3,5) – 6(3,4) A and E lines (Hollis et al. 2001), the 9(4,5) – 8(4,4) P transition (Requena-Torres et al. 2006), the 9(4,5) – 8(4,4) P transition (Requena-Torres et al. 2006) qualify for imaging.

**Table 2**. The Most Uncontaminated Transitions of MF

Rest Frequency	Transition	$E_u$	$\log_{10} \frac{A_{ul}}{s^{-1}}$	$S_{ij}\mu^2$	FWHM	$n_{ m crit}$	P Factor	D Factor	Comments
(MHz)		(K)	3	$(\text{Debye}^2)$	(MHz)	$(cm^{-3})$	(%)	(%)	
84449.169(10)	7(2,6) - 6(2,5) E	19.00	-5.0992	17.0	1.533	1992.9	97.6	79.9	l, h
85185.466(10)	7(5,3) - 6(5,2) A v = 1	220.89	-5.3602	9.1			97.4	63.4	
85186.063(10)	7(5,2) - 6(5,1) A v = 1	220.89	-5.3602	9.1			"	II .	
86027.723(10) <sup>a</sup>	7(5,3) - 6(5,2) E	33.12	-5.3461	9.1			99.6	70.8	
$86029.442(10)^{a}$	7(5,3) - 6(5,2) A	33.11	-5.3459	9.1			"	"	

Table 2 continued on next page

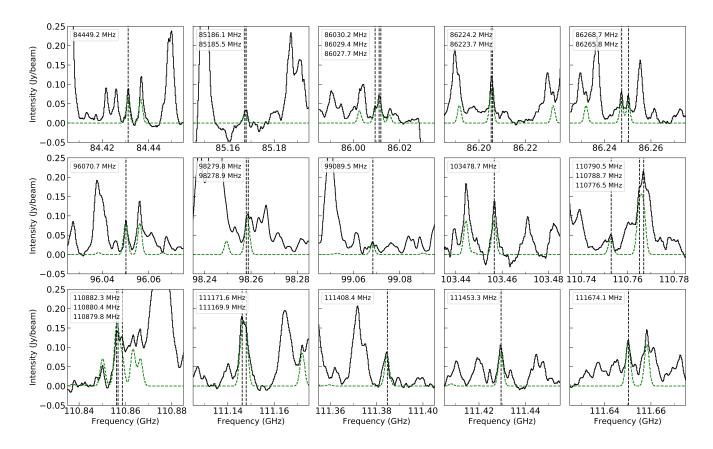


Figure 6. Observed spectra of the 26 transitions of MF with a P factor > 95% and a D factor > 60% toward LMH are plotted in black over the best-fit LTE simulated spectra of MF in green. The observed spectra are extracted from a uniform synthesized beam of  $3.01'' \times 1.47''$ . The observed frequencies in GHz are marked below each panel. The intensities are indicated in Jybeam<sup>-1</sup>.

Table 2 (continued)

Rest Frequency	Transition	$E_u$	$\log_{10} \frac{A_{ul}}{s^{-1}}$	$S_{ij}\mu^2$	FWHM	$n_{ m crit}$	P Factor	D Factor	Comments
(MHz)		(K)		$(Debye^2)$	(MHz)	$(cm^{-3})$	(%)	(%)	
86030.186(10) <sup>a</sup>	7(5,2) - 6(5,1) A	33.11	-5.3459	9.1			"	"	
86223.655(10)	7(4,3) - 6(4,2) E	27.17	-5.2074	12.5			99.3	65.2	
86224.160(10)	7(4,4) - 6(4,3) E	27.16	-5.2075	12.5			"	"	
86265.796(10) <sup>a</sup>	7(3,5) - 6(3,4) A	22.51	-5.1209	15.2	1.739	1707.4	99.7	63.2	h
86268.739(10) <sup>a</sup>	7(3,5) - 6(3,4) E	22.52	-5.1248	15.1	1.800	1635.3	99.7	69.3	1
96070.725(10)	8(2,7) - 7(2,6) E	23.61	-4.9191	19.8	1.940	2712.5	97.7	97.6	l, h
98278.921(10)	8(6,3) - 7(6,2) E	45.13	-5.2179	9.3			96.4	65.3	

Table 2 continued on next page

20 XUE ET AL.

Table 2 (continued)

Rest Frequency	Transition	$E_u$	$\log_{10} \frac{A_{ul}}{\mathrm{s}^{-1}}$	$S_{ij}\mu^2$	FWHM	$n_{ m crit}$	P Factor	D Factor	Comments
(MHz)		(K)		$(Debye^2)$	(MHz)	$(cm^{-3})$	(%)	(%)	
98279.762(10)	8(6,3) - 7(6,2) A	45.13	-5.2179	9.3			11	"	
99089.518(10)	8(3,5) - 7(3,4) A v = 1	215.08	-4.9159	18.2	2.095	2609.9	98.7	64.8	1
103478.663(10)	8(2,6) - 7(2,5) A	24.63	-4.8188	20.0	2.326	3070.6	98.9	63.4	l, h
110776.499(10)	9(1,8) - 8(1,7) A v = 1	215.75	-4.7151	23.1	2.320	4183.4	96.9	68.0	l, h
110788.664(10)	10(1,10) - 9(1,9) E	30.27	-4.7051	26.2			96.6	62.5	
110790.526(10)	10(1,10) - 9(1,9) A	30.26	-4.7049	26.2			"	"	
110879.766(10)	9(3,7) - 8(3,6) E	32.58	-4.7510	21.2			97.1	89.6	
110880.447(10)	9(5,5) - 8(5,4) A	43.16	-4.8592	16.6			"	"	
110882.331(10)	9(5,5) - 8(5,4) E	43.16	-4.8594	16.6			"	"	
111169.903(10)	10(0,10) - 9(0,9) E	30.25	-4.7002	26.2			99.6	82.7	
111171.634(10)	10(0,10) - 9(0,9) A	30.23	-4.7002	26.2			"	"	
111408.412(10) <sup>b</sup>	9(4,5) - 8(4,4) E	37.26	-4.8123	18.2	2.032	3841.2	94.8	86.1	l, h
111453.300(10) <sup>c</sup>	9(4,5) - 8(4,4) A	37.24	-4.7878	19.2	2.681	3081.6	99.9	75.0	l, h
111674.131(10) <sup>b</sup>	9(1,8) - 8(1,7) E	28.14	-4.7037	23.2	2.988	3362.0	99.6	78.7	l, h

Note— Pertinent parameters of the transitions assigned to MF with P > 95% and D > 60% taken from JPL catalog. Here we consider the transitions for both the vibrational ground state and first excited state.  $Q_r = 12.45 \times T_r^{1.5}$  Remijan et al. (2003). P and D factors are calculated based on the observed spectra toward LMH and the simulated spectra assuming an excited temperature of 190 K. "l" and "h" mark the transitions for which the low- and high-velocity components are used for generating the chemical map of MF. The transitions with ditto marks in the column of P and D factors are blended with the transitions in the previous row.

 $CH_2OHCHO$ —In the 84091-114368 MHz frequency range of the EMoCA survey, 402 ground-state transitions of GLA are listed in the CDMS catalog. We focused on the 83 transitions of GLA with S/N > 3 under the simulation condition  $T_{\rm ex} = 190$  K, covering J values up to 18. We found 10 such lines with a P factor > 90% and a D factor > 60% which were assigned to be the transitions of GLA. Table 3 summarizes the 10 most uncontaminated transitions with the pertinent molecular

aLines previously reported in Hollis et al. (2001).

<sup>&</sup>lt;sup>b</sup> Lines previously reported in Requena-Torres et al. (2006).

<sup>&</sup>lt;sup>c</sup>Lines previously reported in Remijan et al. (2003).

parameters and the P and D factors. The spectral lines used in the detection of GLA toward LMH are shown in Figure 7.

As in the case of MF, we studied the three lines of GLA reported by Hollis et al. (2000) and the 12 lines from Halfen et al. (2006). But none of them has consistency factors over our threshold. The observed line intensities of these 11 lines are much higher than the simulated values; this problem is interpreted as serious blending with other molecules. In contrast, the previously unreported 10 transitions, following our criteria, are the most uncontaminated lines identified with GLA at this frequency range toward Sgr B2(N).

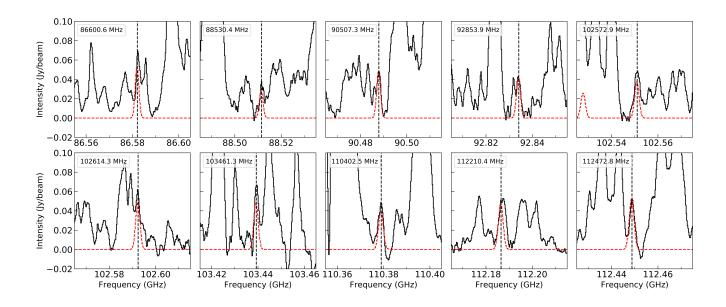


**Figure 7.** Same as Figure 6 for the 10 transitions of GLA. The best-fit LTE simulated spectra of GLA are shown in red.

 $CH_3COOH$ —There are 573 vibrational ground-state transitions of AcA from the SLAIM database in the 84091-114368 MHz spectral range; 136 of AcA transitions have S/N larger than 3 in the simulated spectra with  $T_{\rm ex} = 190$  K including the best known six four-fold degenerate transitions, 90203.35, 90246.26, 100855.43, 100897.46, 11507.27, and 111548.53 MHz lines (Mehringer et al. 1997; Remijan et al. 2003). However, the emission lines of AcA suffer seriously from contamination from other species. The observed intensity of some of the well-known four-fold degenerate transitions of

Table 3. The Most Uncontaminated Transitions of GLA

Rest Frequency	Transition	$E_u$	$\log_{10} \frac{A_{ul}}{\mathrm{s}^{-1}}$	$S_{ij}\mu^2$	FWHM	$n_{ m crit}$	P Factor	D Factor	Comments
(MHz)		(K)		$(Debye^2)$	(MHz)	$(cm^{-3})$	(%)	(%)	
86600.5997(67)	17(5,12) - 17(4,13)	101.14	-4.8624	63.6	1.684	3210.0	91.0	86.6	
88530.4001(46)	8(4,5) - 8(3,6)	29.73	-4.9874	21.7	2.125	1950.2	94.9	68.9	l, h
90507.2610(133)	17(3,14) - 17(2,15)	93.77	-4.9064	50.3	2.012	2536.7	98.1	80.4	1
92853.9487(49)	12(4,9) - 12(3,10)	53.23	-4.8762	35.7	2.231	2517.1	97.2	79.2	1
102572.9391(82)	14(3,12) - 14(2,13)	63.60	-4.8764	30.7	2.960	2094.5	99.0	62.2	l, h
102614.3429(137)	18(3,15) - 18(2,16)	104.10	-4.7784	49.0	2.373	3274.6	97.9	64.4	1
103461.3106(66)	15(4,12) - 15(3,13)	76.75	-4.7501	42.8	2.102	3979.1	95.0	77.7	h
110402.5367(87)	15(3,13) - 15(2,14)	71.79	-4.8048	31.0	2.549	3087.6	99.4	80.3	h
112210.4422(52)	12(5,8) - 12(4,9)	58.62	-4.6471	34.3	3.638	3161.2	92.2	70.7	l, h
112472.7946(50)	14(5,10) - 14(4,11)	73.76	-4.6197	42.0	2.524	4862.7	98.6	98.4	1

Note— Pertinent parameters of the transitions assigned to GLA with P > 90% and D > 60% are taken from CDMS catalog. Here we only consider the transitions for vibrational ground state.  $Q_r = 6.868 \times T_r^{1.5}$  is derived from the partition function at different temperatures given in CDMS. P and D Factors are calculated based on the simulated spectra assuming the excited temperature as 190 K. "l" and "h" mark the transitions of which the low- and high-velocity components are used for generating the chemical map of GLA respectively.

AcA, for example 9(\*,9)-8(\*,8) A at 100897.46 MHz where asterisks can be 0 or -1, are much higher than their simulated intensity and the observed intensity of their corresponding E pairs in spite of their similar upper-level energy.

There are only three transitions of AcA over the threshold P factor > 90% and D factor > 60% with S/N > 3 as shown in Table 4. If we go to weaker lines, there are two more transitions of AcA satisfying the requirement of the consistency factors but with lower S/N. They are the 23(15,9) - 23(14,10) transition with  $S/N \sim 2.7$  and the 24(-13,11) - 24(-12,12) transition with  $S/N \sim 2.6$ . The relatively high values of the consistency factors and the similar spatial distribution of these two transitions with that of the three stronger lines make their assignments reliable. Therefore, we image the transition maps of the five transitions shown in Table 4. Figure 8 shows the observed and simulated spectra of these transitions toward the LMH region.

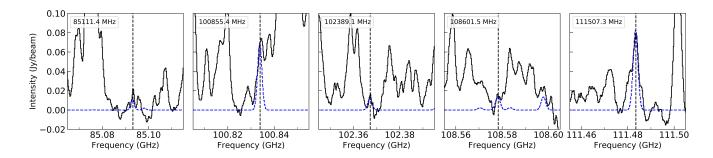


**Figure 8.** Same as Figure 6 for the five transitions of AcA. The best-fit LTE simulated spectra of AcA are shown in blue.

Table 4. The Most Uncontaminated Transitions of AcA

Rest Frequency	Transition	$E_u$	$\log_{10} \frac{A_{ul}}{\mathrm{s}^{-1}}$	$S_{ij}\mu^2$	FWHM	$n_{ m crit}$	P Factor	D Factor	Comments
(MHz)		(K)		$(Debye^2)$	(MHz)	$(cm^{-3})$	(%)	(%)	
85111.3900(30)	23(15,9) - 23(14,10)	251.54	-5.3344	30.3	1.201	1491.4	95.9	65.7	1
$100855.4300(10)^{a}$	$9(*,9) - 8(*,8) E^{a}$	25.67	-4.5116	49.0	3.450	4092.4	94.7	70.7	1
102389.0800(10)	24(-13,11) - 24(-12,12)	266.21	-5.1281	29.2	1.544	2244.7	96.7	86.0	1
108601.4600(10)	21(-10,11) - 21(-9,12)	199.07	-5.1076	22.5	2.008	1919.4	90.1	82.6	
$111507.2800(10)^{\mathrm{b}}$	$10(*,10) - 9(*,9) E^{a}$	31.02	-4.3757	54.8	3.037	7029.4	99.4	86.7	

Note— Pertinent parameters of the transitions assigned to AcA with P > 90% and D > 60% are taken from SLAIM catalog. Here we only consider the transitions for vibrational ground state.  $Q_r = 14.10 \times T_r^{1.5}$  Remijan et al. (2003). P and D Factors are calculated based on the simulated spectra assuming the excited temperature as 190 K. "l" marks the transitions that are most uncontaminated and of which the low-velocity component is used for generating the chemical map of AcA respectively. Each of the fourfold degenerate transitions consists of two a-type and two b-type degenerate transitions, and is shown with the K quantum numbers as substituted by an asterisk.

Pertinent line parameters of all the detectable transitions of the isomeric species of  $C_2H_4O_2$  observed in this survey with signal to noise ratio (S/N) larger than  $\sim 3$  are summarized in Appendix Tables 6, 7 and 8 respectively.

 $<sup>^</sup>a$ Fourfold transition detected by Mehringer et al. (1997); asterisk could be 0 or -1.

<sup>&</sup>lt;sup>b</sup> Fourfold transition detected by Remijan et al. (2003); asterisk could be 0 or 1.

To more accurately determine the excitation temperature, we perform a  $\chi^2$  fitting over these less contaminated transitions to statistically determine  $T_{ex}$  toward the LMH region. The formula for  $\chi^2$  is defined as:

$$\chi^2 = \sum_{i=1}^n \frac{(I_{\text{obs},i} - I_{\text{sim},i})^2}{\sigma^2},\tag{3}$$

where  $I_{\rm sim}$  and  $I_{\rm obs}$  represent the simulated peak intensity and the observed values at the corresponding frequency respectively, and  $\sigma$  is the rms noise level of the observed spectrum.

For MF, a  $T_{\rm ex}$  of 201(12) K and a  $N_{T,MF}$  of  $1.18(0.05) \times 10^{17}$  cm<sup>-2</sup> minimized the  $\chi^2$  to 314.6 with the number of degrees of freedom of 15 and yield the best fit. The  $\chi^2$  fitting over these 10 GLA transitions suggested that a  $T_{\rm ex}$  of 146(25) K and a  $N_{T,GLA}$  of  $1.57(0.12) \times 10^{16}$  cm<sup>-2</sup>, which minimized the  $\chi^2$  to 14.7 with the number of degrees of freedom of 8, best fit the observation data. A result of  $T_{\rm ex} = 296(59)$ K and  $N_{T,AcA} = 4.63(0.92) \times 10^{16}$  cm<sup>-2</sup> is obtained by  $\chi^2$  fitting using the five AcA transitions. The minimum value of  $\chi^2$  is 3.3 with a degree of freedom of 3.

Based on the ALMA Band 3 observations, the best fit to the observed spectra toward LMH in this study suggests abundance ratios of MF, AcA, and GLA [HCOOCH<sub>3</sub>]:[CH<sub>3</sub>COOH]:[CH<sub>2</sub>OHCHO] of  $\sim$  7.5:2.9:1. Although this result is in agreement with the suggested ratio of [HCOOCH<sub>3</sub>]:[CH<sub>2</sub>OHCHO]  $\sim$  6.7 observed with the OVRO array (Hollis et al. 2000), we find an enhancement of the abundance of AcA with respect to those reported by Remijan et al. (2002). In Remijan et al. (2002), the observations conducted with the OVRO array reported an MF to AcA abundance ratio, [HCOOCH<sub>3</sub>]:[CH<sub>3</sub>COOH], of (16 - 32):1 toward the LMH region. Based on a uniform analysis of observations with the IRAM 30m telescope, Belloche et al. (2013) suggest that  $T_{\rm ex}=80~{\rm K}$  and  $N_{T,MF}=4.37\times10^{17}~{\rm cm}^{-2}$  with a source size of 4.0" for MF;  $T_{\rm ex}=80~{\rm K}$  and  $N_{T,GLA}=1.8\times10^{15}~{\rm cm}^{-2}$  with a source size of 10.0" for GLA; and  $T_{\rm ex}=100~{\rm K}$  and  $N_{T,AcA}=1.05\times10^{16}~{\rm cm}^{-2}$  with a source size of 4.0" for AcA, based on which the abundance ratios among the three molecules are [HCOOCH<sub>3</sub>]:[CH<sub>3</sub>COOH]:[CH<sub>2</sub>OHCHO]  $\sim$  242:5.8:1. The inconsistency between the two values for [HCOOCH<sub>3</sub>]:[CH<sub>3</sub>COOH]:[CH<sub>2</sub>OHCHO] can be justified in part by the different observations and data processing methods. The 30m IRAM observation has beam sizes larger than 11" and, therefore, cannot constrain the source sizes of the three molecules. In addition, the rotational diagram method

that Belloche et al. (2013) used to determine column density requires a large number of the less contaminated transitions covering a large range of energy levels. But the detected AcA transitions in Belloche et al. (2013) have a narrow range of energy levels,  $E_l$  of 16-25 K, and there are only 5 detected GLA transitions, which could introduce large uncertainties to the results. In contrast, in our study, we are more rigorous with line contamination and use  $\chi^2$  fitting to constrain the excitation temperature. In addition, the small synthesized beam sizes of the ALMA observations resolve the source sizes of the three molecules well.

#### 4. RESULTS

In order to determine the velocity components of the three isomers, we examined the spectral transitions of the three isomers as extracted from an aperture with a diameter of 11" and covering most of the continuum emission region. Figure 9 shows the thermal dust continuum map of the Sgr B2(N) region as obtained with ALMA Band 3 observations at 85.9 GHz along with the LMH, N1, N2 and N3 emission cores (Belloche et al. 2016; Bonfand et al. 2017) which will be referenced below. The average systemic  $V_{lsr}$  of the N1 core is  $\sim 64$  km s<sup>-1</sup> while that for N2 and N3 is  $V_{lsr} \sim 73$ .

In the most unblended spectral transitions within an aperture comparable to the size of the major continuum emission region, MF has two emission features at two different systemic velocities,  $V_{lsr} \sim$  64 and 73 km s<sup>-1</sup>. The velocity constitution of MF is consistent with the findings in Belloche et al. (2016) and Bonfand et al. (2017). In contrast to Belloche et al. (2013), who did not detect the high-velocity component of GLA toward Sgr B2(N) with the IRAM 30m line survey, two velocity components of GLA are also identified in our study. This difference from our result could be explained by the low sensitivity of the IRAM telescope due to beam dilution and smaller total collecting area. ALMA's high angular resolution and sensitivity give us a better understanding of the velocity components of these LAMs. In contrast to MF and GLA, however, AcA had only a single velocity component near 64 km s<sup>-1</sup> resolved. There is no AcA emission above  $1\sigma$  around the N2 or N3 regions for any AcA transitions.

## 4.1. Transition Maps

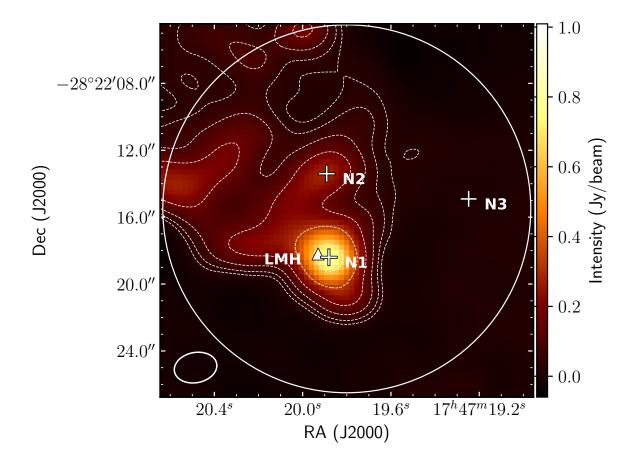


Figure 9. Continuum map of the Sgr B2(N) region obtained with EMoCA survey at 85.9 GHz (Belloche et al. 2016; Bonfand et al. 2017). Contour levels start at five times the rms noise level (4.1 mJy/beam) and double in value up to the peak value. The solid circle shows the aperture  $(11'' \times 11'')$  from which the spectra was extracted from to examine the velocity components of the three isomers. The triangle marker shows the LMH region.

We carried out an intensive study on the spatial mapping of the  $C_2H_4O_2$  isomeric family with the most uncontaminated transitions that were discussed in Sec 3.2. We generated peak intensity images (i.e. moment-8 map) for the least contaminated transitions of the  $C_2H_4O_2$  isomeric species and refer to them as transition maps. For MF and GLA, we imaged each of the transitions near the two systemic velocity components separately. For the low-velocity component, the integrated velocity

range is 59-68 km s<sup>-1</sup> while for the high-velocity component, the range is 70-75 km s<sup>-1</sup>. For AcA, only the one velocity range, 59-67 km s<sup>-1</sup>, was imaged.

 $HCOOCH_3$ —For MF, we imaged the emission from the 10 most uncontaminated transitions with P factor > 95 and D factor > 60, over a range of upper-state energies from 23 K to 221 K. The peak intensity images of the low-velocity component and high-velocity component are shown in Figure 10 and 11 respectively. In Figure 10 and 11, the background color images are the 85.9 GHz continuum of the Sgr B2(N) region. The contours indicate the location of the MF emission of each transition. As the most uncontaminated transitions are selected based on the spectrum toward LMH only, some of these MF lines still suffer from spatial contamination, as summarized in the captions of Figure 10 and 11.

Despite the spatial contamination, based on the peak intensity images of MF, it is clear that different transition maps of MF show nearly identical spatial distributions to each other at each characteristic velocity over a range of excitation levels. We identified two cores of emission of the low-velocity component and two of the high-velocity component among all the transition maps in 10 and 11. The low-velocity component has a extended distribution which is offset from the continuum emission peak. The distribution of the emission cores of MF is described more completely in Section 4.2 in a quantitative way using its chemical map, which is, in short, a weighted composite transition map.

As outlined in Brouillet et al. (2015), the spatial distributions from interferometric observations were suggested to be similar among transitions with similar excitation conditions. However, we find that the morphology of MF is consistent across a wide range of upper-state energy levels; i.e., the intensity maps obtained from v = 0 and v = 1 of MF are similar.

 $CH_2OHCHO$ —We generated the interferometric images of the 10 least blended GLA transitions with upper-state energy levels ranging from 22 K to 64 K for both the low-velocity and high-velocity components, as shown in Figures 12 and 13, respectively. In contrast to MF, there is substantial con-

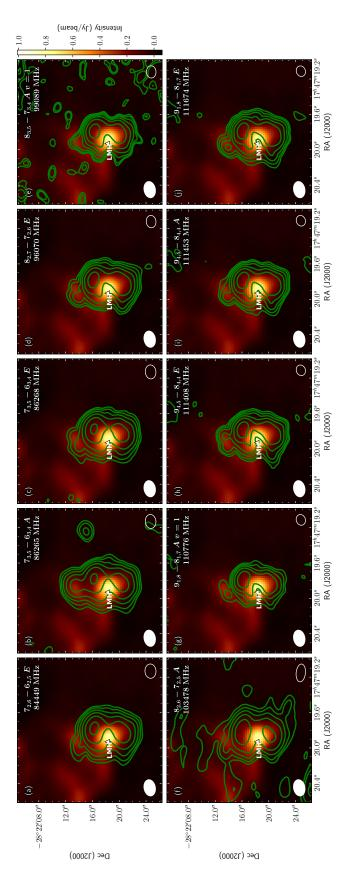


Figure 10. Peak intensity images of the low-velocity component (64 km s<sup>-1</sup>) of the 10 MF transitions overlaid on the continuum emission at 85.9 GHz (background color image). The integrated velocity range of the low-velocity component ranges from 59 to 68 km s<sup>-1</sup>. The MF contours start at  $3\sigma$  and double in value up to the peak value. Most of transitions of MF show consistent morphology. Spatial contamination source: panel (b) is contaminated with the high-velocity component of the MF 7(3,5) - 6(3,4) E transition at 86265 MHz.

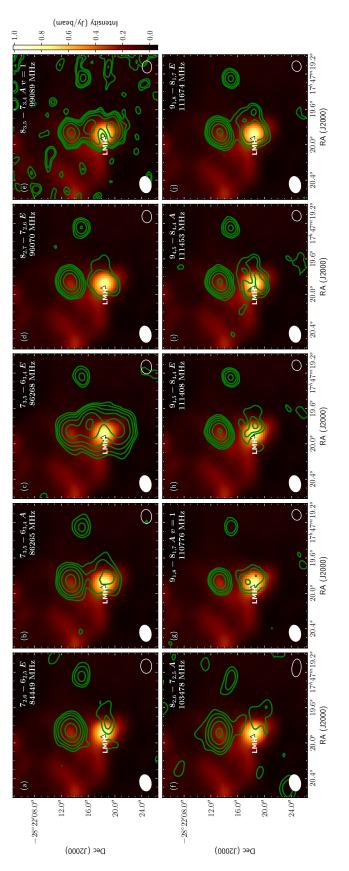


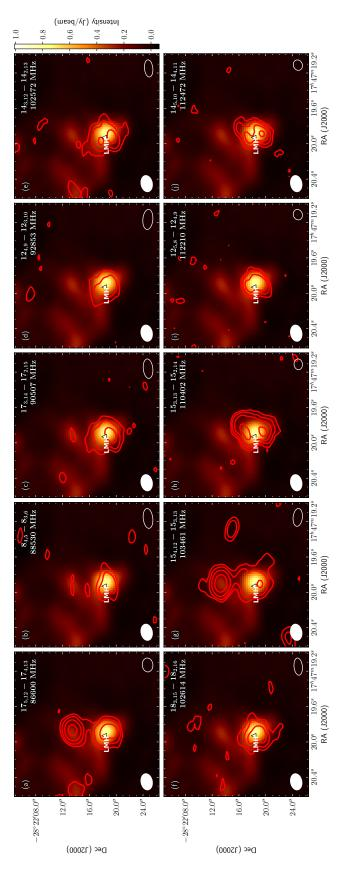
Figure 11. Peak intensity images of the high-velocity component (73 km s<sup>-1</sup>) of the 10 MF transitions overlaid on the continuum emission at 85.9 GHz (background color image). The integrated velocity range of the high-velocity component ranges from 70 to 75 km s<sup>-1</sup>. The MF contours start at  $3\sigma$  and double in value up to the peak value. We resolve the high-velocity component as the second velocity-component of MF. Spatial contamination sources: panel (c): the low-velocity component of the MF 7(3,5)-6(3,4) A transition at 86265 MHz; panel (e): the thioformal dehyde  $(H_2^{13}CS)$  3(2,1)-2(2,0) transition at 99086 MHz.

tamination among the spatial distributions of GLA. While the LMH region line profiles are relatively clean, the N2 region suffers much more significantly from this.

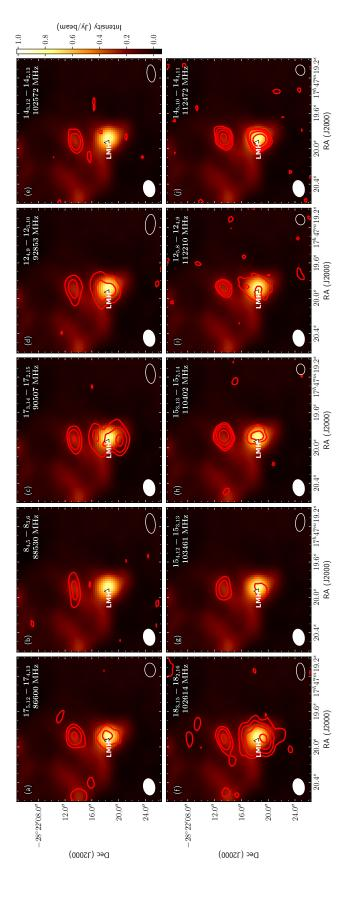
Despite the contamination mentioned above, the remaining peak intensity images of GLA are consistent with each other, including the low-velocity components of seven transitions which are marked with "l" in Table 3 and the high-velocity components of four transitions marked with "h" in Table 3 respectively. From the uncontaminated transitions, as evident in Figures 12 and 13, we resolved one emission core from the low-velocity component of GLA with a source size smaller than 7" and one from the high-velocity component with a source size  $\sim 4$ ". The emission regions of GLA are more compact that those of MF. A detailed comparison of the distributions of the isomers is discussed in Section 4.2.

The result of a compact emission region of GLA is in contradiction with previous research on the spatial distribution of GLA. Hollis et al. (2001) mapped the 8(0,8) - 7(1,7) transition of GLA at 82470.67 MHz with the BIMA array and suggested an extended distribution of GLA toward Sgr B2(N) with a source size of around 60 ". The difference found between the distributions from our study may be due to the contamination of the transition detected by Hollis et al. (2001). In their study, only one transition was mapped. Therefore, they could not distinguish if the transition was contaminated by comparing maps from different transitions which is what we do in the present study. In addition, the broad line width of the GLA 8(0,8) - 7(1,7) transition imaged by Hollis et al. (2001), 24.3 km s<sup>-1</sup>, compared with 8.2 km s<sup>-1</sup> for the MF line in their observations is also consistent with the existence of contamination. Thus, the conclusions reached by Hollis et al. (2001) are most likely inaccurate given the fact that it is probably based on a blended transition of GLA.

 $CH_3COOH$ —Figure 14 shows the peak intensity images of AcA for the five transitions listed in Table 4. The upper-state energy levels range from 26 to 266 K. Because there is no emission with S/N > 1 in the  $\sim 73$  km s<sup>-1</sup> regions, we only resolve one low-velocity component of AcA (64 km s<sup>-1</sup>). In addition to the limited number of clean emission transitions, AcA also suffers from severe spatial contamination. The least contaminated three transitions are marked with "l" in Table 4.



acetone ((CH<sub>3</sub>)<sub>2</sub>CO) 19(10,10)-19(9,11) AA transition at 86604.63 MHz, and the gauche-ethanol (g-CH<sub>3</sub>CH<sub>2</sub>OH) 5(3,3) - 4(3,2) transition Figure 12. Peak intensity images of the low-velocity component (64 km s<sup>-1</sup>) of the 10 GLA transitions overlaid on the continuum emission at 85.9 GHz (background color image). The integrated velocity range of the high-velocity component ranges from 59 to 68 km s<sup>-1</sup>. The shows consistent distribution among different transitions. Spatial contamination sources: panel (a): the high-velocity components of the GLA contours start at  $3\sigma$  and double in value up to the peak value. Despite the transitions suffering from spatial contamination, GLA at 86604.34 MHz; panel (g): the high-velocity component of MF 8(2,6) - 7(2,5) E at 103466 MHz; panel (h): the (CH<sub>3</sub>)<sub>2</sub>CO 6(5,2)-5(4,1)EE transition at 110401 MHz.



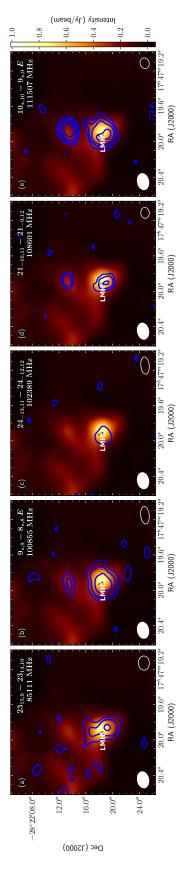
The GLA contours start at  $3\sigma$  and double in value up to the peak value. We resolve the high-velocity component near the N2 region as the second velocity-component of GLA. Spatial contamination sources: panel (a): a weak and unidentified emission feature; panel (c): a strong **Figure 13.** Peak intensity images of the high-velocity component (73 km s<sup>-1</sup>) of the 10 GLA transitions overlaid on the continuum emission at 85.9 GHz (background color image). The integrated velocity range of the high-velocity component ranges from 70 to 75 km s<sup>-1</sup>. emission from g-CH<sub>3</sub>CH<sub>2</sub>OH 6(2,5) - 5(1,5) at 90503 MHz; panel (d): unidentified; panel (f): unidentified; panel (j): the low-velocity component of the strong emission feature from the formic acid (HCOOH) 5(3,2) - 4(3,1) transition at 112467 MHz.

Given these limitations, the morphology of AcA cannot be accurately determined based on the limited number and the spatial contamination of the transition maps. But we can still see that the emission peaks are co-spatial among all the transition maps. Besides, Mehringer et al. (1997) mapped Sgr B2(N) with the OVRO array in two transitions of AcA at 90246 MHz and 100855 MHz and Remijan et al. (2002) did the same at 111507 MHz and 111547 MHz. Although the two transitions, 90246 MHz and 111547 MHz, are are known to be contaminated toward LMH and the distribution of the transition at 111507 MHz is spatially contaminated toward the N2 region, the AcA emission peak resolved with the previous observations is consistent with our study. The peak positions are all at  $\alpha_{J200} = 17h47m19.9(0.1)s$ ,  $\delta_{J2000} = -28^{\circ}22'19(1)''$  within 1 " which confirms the assertion that the AcA lines are coming from a common source (Remijan et al. 2002).

# 4.2. Chemical Maps of $C_2H_4O_2$

Because the uncontaminated transitions covering an extensive range of upper-state energies show similar morphology, the effect of excitation conditions is ruled out and the morphology of these transition maps is determined by the true distribution of molecules. For this reason, with an increased number of unblended transitions with similar morphologies, we can combine the transition maps to achieve mm chemical maps for the  $C_2H_4O_2$  isomers. A chemical map is obtained by stacking the peak intensity images of transitions which are mostly free of contamination. In the stacking process, we used the inverse-variance weighting for each transition, where the variance is the square of the noise of each data cube. Compared with a single transition map, the chemical map allows us to infer molecular distributions at a high S/N. It is worthwhile noting that the ultimate units of the chemical map are non-physical and thus nothing should be inferred from the value of intensity directly.

For MF, we stacked the peak intensity images of the nine least contaminated transitions marked with "l" in Table 2 to obtain the low-velocity component and the eight transitions marked with "h" in Table 2 for the high-velocity component of the chemical map of MF. Figure 15 (left panel) shows the chemical maps of MF in green with solid lines representing the low-velocity component and dashed lines the high-velocity component over the 85.9 GHz continuum emission. Compared with transition maps, we can better quantify the distribution of the emission cores with the chemical map. In the



high-velocity component of a transition with a rest frequency of  $\sim 108606$  MHz, of which the low-velocity component was also observed The integrated velocity range of the high-velocity component ranges from 59 to 67 km s<sup>-1</sup>. The AcA contours start at  $3\sigma$  and double in by the high-velocity component of the GLA transition 24(7,18) - 23(8,15) at 100859 MHz; panel (d) is probably contaminated by the Figure 14. Peak intensity images of the five AcA transitions overlaid on the continuum emission at 85.9 GHz (background color image). value up to the peak value. We only resolved one velocity component of AcA  $((\sim 64 \text{ km s}^{-1}))$  and have limited number of the transition maps of AcA. Spatial contamination sources: panel (b) is contaminated by a weak emission feature toward the N2 region contributed toward LMH as a strong emission line. However, this transition is not found in any public database and, as such, remains unidentified; panel (e) is contaminated by the high-velocity component of the overlapping transitions of trans-ethanol (t-CH<sub>3</sub>CH<sub>2</sub>OH)-12(7,6) - 13(6,7)and 12(7,5) - 13(6,8))-at 111510 MHz in the north region.

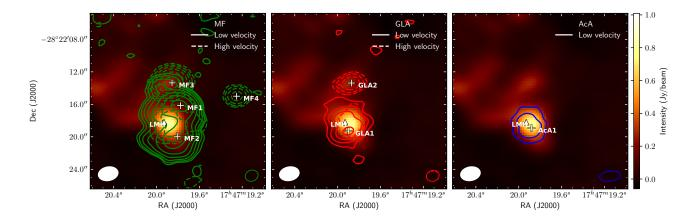


Figure 15. Emission contours from the chemical maps of MF (left), GLA (middle) and AcA (right) overlaid on the continuum emission at 85.9 GHz (background color image) toward Sgr B2(N). The solid lines represent the low-velocity component, while the dashed lines correspond to the high-velocity component. The contour levels start at  $5\sigma$  and double in value up to the peak value, with  $\sigma \sim 1.7$  mJy beam<sup>-1</sup> for MF,  $\sim 2.0$  mJy beam<sup>-1</sup> for GLA and  $\sim 2.5$  mJy beam<sup>-1</sup> for AcA. The emission cores of each molecule are marked by a cross and labeled MF<sub>NUMBER</sub>, GLA<sub>NUMBER</sub> and AcA<sub>NUMBER</sub> correspondingly.

chemical map of MF, four distinct emission cores of MF are resolved. The low-velocity component contains two emission cores marked as MF1 and MF2, which are connected with each other over a distance of 3.8" and located within the cloud. The other two emission cores, MF3 and MF4, with high velocity, are separated by around 8.1". The coordinates of the four cores are summarized in Table 5. The overall distribution of MF is offset from the continuum emission and more extended than that of GLA and AcA. The two emission peaks of MF with low velocity are offset from LMH by  $\sim 2.9$ " for MF1 and  $\sim 2.4$ " for MF2 respectively, while MF3 and MF4 are spatially coincident with the N2 core and N3 core defined in Bonfand et al. (2017), respectively.

The chemical map of GLA is represented in Figure 15 (middle panel), which is stacked with the transition maps of the seven transitions marked with "l" in Table 3 for the low-velocity component and the four transitions marked "with h" in Table 3 for the high-velocity component. With the chemical map of GLA, we can better examine the spatial distribution features of GLA that are not clearly resolved in its transition maps. GLA also has distinct high- and low- velocity components. For the low-velocity component, we locate the major emission core (GLA1) at  $\alpha_{J200} = 17h47m19.9s$ ,

**Table 5.** Positions of the LMH Region and the Molecular Emission Peaks of the  $C_2H_4O_2$  isomers

Source	Coor	$V_{ m lsr}$	
	$17^h47^m$	$-28^{\circ}22'$	$\rm km\ s^{-1}$
LMH(centroid)	$19.930^{s}$	18.200"	64
MF1	$19.776^{s}$	$16.158^{\prime\prime}$	64
MF2	$19.806^{s}$	$19.934^{\prime\prime}$	64
MF3	$19.855^{s}$	$13.357^{\prime\prime}$	73
MF4	$19.252^{s}$	$15.002^{\prime\prime}$	73
GLA1	$19.899^{s}$	$19.294^{\prime\prime}$	64
$\operatorname{GLA2}$	$19.871^{s}$	$13.379^{\prime\prime}$	73
AcA1	$19.881^{s}$	18.926"	64

 $\delta_{\rm J2000} = -28^{\circ}22'19.3''$  and resolve an extended feature to the north-east. An emission core with high velocity (GLA2) is resolved and co-spatial with the MF3 core. GLA2 is  $\sim 5.9''$  north of GLA1. Compared with MF, the distribution of GLA is more compact and spatially consistent with the continuum emission. The GLA1 core is offset from the LMH peaks by only  $\sim 1.2''$  while the GLA2 core is co-spatial with the N2 continuum emission core (Bonfand et al. 2017).

Each of the transition maps of AcA are quite different from each another, perhaps due to the low S/N of the most uncontaminated lines. The difference, as well as the limited number of the unblended transitions, 5 in total, make the morphology of AcA difficult to characterise. But, we can gain insight as to its distribution by looking at its chemical map with increased S/N. In the chemical map of AcA as shown in Figure 15 (right), AcA only emits from the region within the low-velocity cloud and has one emission core (AcA1). We do not resolve any high-velocity component for AcA. In addition, the emission region of AcA appeared to be, interestingly, coincident with the distribution of the low-velocity component of GLA, and the spatial separation of AcA1 and GLA1 is smaller than 0.5". As with GLA, we find the emission region of AcA to be compact and spatial coincident with the continuum emission. AcA1 is offset from the LMH peaks by only  $\sim 1.0$ ".

### 5. DISCUSSION

Our observations indicate that the three isomers of  $C_2H_4O_2$  have distinct morphologies, as shown in Figure 15. The question remains as to why the three isomers have such different distributions compared to each other despite their identical atomic composition. Here, we discuss the possible mechanisms that could contribute to this difference.

Although different observations could bias the result of imaging and contribute to spatial difference, this is not the case in our study. Because we self-consistently analyzed these three isomers in the same observations, we can rule out any differences caused by observations with different facilities, techniques, or frequency regimes. Instead, there are both physical and chemical causes, which could be interwoven, to explain the spatial difference.

Different physical conditions and therefore different excitation conditions inside the source might lead to the diversity in morphology. While our best fit to the observed data suggests the  $T_{\rm ex}$  of MF toward LMH to be  $\sim 200$  K, Bonfand et al. (2017) derived a similar  $T_{\rm ex}$ ,  $\sim 150$  K, toward both N2 and N3, the two high-velocity cores. Because the transition maps of each molecule are spatially similar across a large range of upper-state energy levels, we can largely rule out the excitation temperatures of the multiple components of Sgr B2(N) as the source of the distinct distributions. In addition, the three species are similar in terms of both photo-absorption cross-sections and ionization potentials (Puletti et al. 2010). Therefore, selective photo-destruction fails to account for the differentiation in these morphologies. Regarding cloud density, Sánchez-Monge et al. (2017) characterized the small scale structures of Sgr B2(N), which include the cores associated with the seven molecular emission peaks of the three isomers, with various hydrogen densities in a range of  $10^7 - 10^9$  cm<sup>-3</sup>. To estimate  $n_{\rm crit}$ , we adopted a typical H<sub>2</sub> collisional cross section  $\sim 10^{-15}~{\rm cm}^2$  (Condon & Ransom 2016). Compared with  $n_{\text{crit}}$  of the  $C_2H_4O_2$  transitions listed in Table 2, 3 and 4, we indeed find  $n_{\rm H_2} > n_{\rm crit} \sim 10^3 {\rm cm}^{-3}$  for the detected lines so that the transitions are probably all thermalized. We also noticed that absorption by the extended material in the cold envelope can cause the offset of MF from the continuum emission peak and should not be neglected. Finally, evolving source properties

38 Xue et al.

with time may contribute to the differences in their spatial distributions. A more thorough analysis of other physical properties of the sources would provide further insights into addressing this point.

The morphological differences among the C<sub>2</sub>H<sub>4</sub>O<sub>2</sub> isomeric family could be explained in part by the difference in their production mechanisms and the large energy barriers for the isomerization among them. The grain surface formation routes originally suggested by Garrod & Herbst (2006) and Garrod et al. (2008) are accepted as the most likely mechanisms to efficiently form LAMs during the warm-up phase of the hot cores. Because thermal desorption is efficient in a warm region, a compact distribution of warm molecules toward hot cores is usually associated with a grain-surface formation scheme followed by thermal desorption, although, as discussed below, gas-phase synthesis cannot be ruled out. In this scenario, the HCO radical becomes mobile on grain surfaces and then reacts with the CH<sub>3</sub>O radical to form HCOOCH<sub>3</sub> or with the CH<sub>2</sub>OH radical to form CH<sub>2</sub>OHCHO. Recent laboratory studies show that H-atom addition and abstraction reactions in ice mantles can lead to more reactive intermediates, which enhance the probability to form MF and GLA through radical-radical recombination (Chuang et al. 2016). Although the grain-surface formation routes of MF and GLA are similar, as both involve HCO, the observed abundances of MF and GLA may be influenced by the abundance difference of the CH<sub>3</sub>O and CH<sub>2</sub>OH radicals on grain surfaces, which, as of vet, have not been measured. Although direct measurements of the abundances of CH<sub>3</sub>O and CH<sub>2</sub>OH on grain by IR absorption lines will be difficult to achieve, indirect determinations could be based on possible future observation of gaseous CH<sub>2</sub>OH and chemical models.

While the radical-radical reactions of MF and GLA only involve primary radicals, Garrod et al. (2008) suggested that AcA is assembled from the OH radical and the CH<sub>3</sub>CO radical. Different from the dominant primary radicals, the CH<sub>3</sub>CO radical, which is a secondary radical, is weakly produced and becomes mobile at higher temperatures than primary radicals due to its complexity (Garrod et al. 2008). The involvement of the CH<sub>3</sub>CO radical makes the AcA formation route different from its structural isomers.

If the scenario of radical-radical reactions on grain surfaces (Garrod et al. 2008) is the main formation mechanism of the three isomers, it is reasonable to expect that the spatial distribution of MF

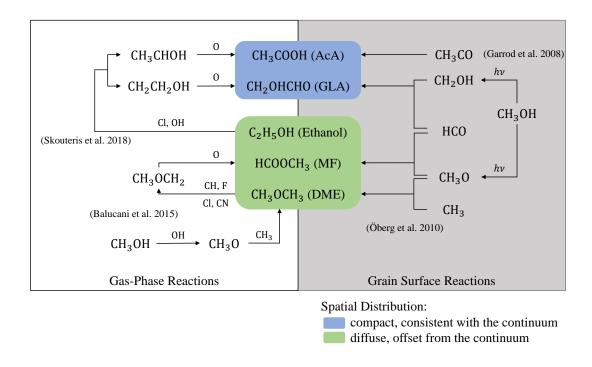


Figure 16. Schematic diagram of the prevalent formation mechanisms related to the  $C_2H_4O_2$  isomers.

and GLA would be similar to each other, since their precursors are HCO and the isomeric radicals that both form from methanol photolysis (Laas et al. 2011), but different from that of AcA. However, the spatial separation of gaseous MF from its isomers and the spatial coincidence of gaseous GLA and AcA make this scenario insufficient for an overall explanation of the observational result. Additionally, there are other pathways involving other surface radicals to form GLA and AcA. GLA could also be formed from the reactions of the HCO radical with the H<sub>2</sub>CO and H on grain surfaces (Beltrán et al. 2009), which was suggested to be the most probable formation mechanism of GLA at low temperature (Woods et al. 2012). Bennett & Kaiser (2007) also proposed that AcA could form via the association reaction of the HOCO radical and the CH<sub>3</sub> radical on grains. But the effectiveness of these proposed pathways is still not fully understood and requires further studies.

In addition to grain chemistry, it was suggested that MF could be also formed via gas-phase processes (Laas et al. 2011; Balucani et al. 2015). Balucani et al. (2015) outlined a possible mechanism for the synthesis of MF with gas-phase reactions in cold environments. Therefore, it is a natural

40 XUE ET AL.

outcome that molecules formed in the gas possess extended distributions (Hollis et al. 2001) but there remains the exception that non-thermal desorption can eject molecules formed on cold grain surfaces into a cold gas, as for the case of methanol formation (Watanabe & Kouchi 2002). Nevertheless, in the gas-phase model, dimethyl ether (CH<sub>3</sub>OCH<sub>3</sub>, DME) works as the precursor of MF via the loss of a hydrogen atom to form the CH<sub>3</sub>OCH<sub>2</sub> radical followed by reaction with atomic oxygen. In addition, an up-to-date scheme for the gas-phase synthesis of GLA and AcA was proposed, where GLA and AcA were both formed from ethanol (CH<sub>3</sub>CH<sub>2</sub>OH) (Skouteris et al. 2018). With H-abstraction from ethanol, two different reactive radicals, CH<sub>2</sub>CH<sub>2</sub>OH and CH<sub>3</sub>CHOH, form and further react with atomic oxygen to produce GLA and AcA respectively. Based on this formation scheme involving ethanol, Skouteris et al. (2018) predicted a higher abundance of AcA than GLA, which agrees well with our findings.

As a test of the different gas-phase formation pathways, the distributions of the chemical precursors could work as proxies to interpret the different morphology of these isomeric and related interstellar molecules. If there are either correlations or anti-correlations between the spatial distributions of the precursors and those of the corresponding products, that could be evidence to support the related chemistry. Therefore, we further imaged the chemical maps of the two proposed precursors, DME and ethanol, involved in the gas-phase reactions. We find that DME is co-spatial with MF, which is consistent with their distributions toward another star formation region, Orion KL (Brouillet et al. 2013). The correlation of MF and DME could also be explained with the common precursor, the surface CH<sub>3</sub>O radical, in their grain-surface formation pathways (Öberg et al. 2010). We also suspect that ethanol, the precursor of GLA and AcA, should have a similar distribution to GLA and AcA. However, the distribution of ethanol is co-spatial to MF and DME proving that no relationship between the triplet of C<sub>2</sub>H<sub>4</sub>O<sub>2</sub> and the proposed gas-phase precursors could be determined.

Different desorption behaviors of the three isomers could also contribute to the spatial separation between MF and the other isomers. In the warm-up model, desorption begins at different temperatures (Garrod et al. 2008). Thus, temperature, which can be a substitute for time in the model, could be related to differing distributions. Burke et al. (2015) found via a Temperature Programmed

Desorption (TPD) analysis that MF desorption starts at a lower temperature,  $\sim 70$  K, compared with the desorption of the other two isomers,  $\sim 110$  K. This different behavior during the thermal processing could account for the extended distribution of MF compared with GLA and AcA. A neglected drawback with the analysis presented in Burke et al. (2015), however, is that they assumed identical grain-surface abundances of the isomers. To connect the effect of the desorption property to the morphological features, taking into account a chemical model, with which the abundances of the isomers could be constrained, seems to be required.

Future research is essential to understand the relative role of the gas-grain chemistry of these three isomers of  $C_2H_4O_2$ . By carrying out detailed model calculations, involving both grain-surface reactions and the newly proposed gas phase pathways of these three molecules (Balucani et al. 2015; Skouteris et al. 2018), we hope to constrain the formation mechanisms of the isomers. Observations of the  $C_2H_4O_2$  and other isomers toward a large sample of interstellar sources could help to constrain the relative importance of their formation pathways and explain the spatial distribution of different molecular isomers.

#### 6. SUMMARY

In this paper, we report an intensive spectral and morphological analysis of the  $C_2H_4O_2$  isomers towards Sgr B2(N) with sensitive ALMA Band 3 observations (Belloche et al. 2016).

We developed quantitative methods to identify weak and mostly uncontaminated transitions which are critical to automatically detect interstellar molecules within a source that has a dense spectrum and a high level of spectral confusion. From these methods, we identified the 26 least contaminated transitions for MF, 10 for GLA and 5 for AcA and further imaged the peak emission maps of these clean transitions. We stacked all of the consistent transition maps of each molecule to obtain their chemical maps, which show more reliable distributions of the molecules with higher S/N ratios.

From the high spatial resolution millimeter chemical maps of the three isomers, we find that they have distinct morphologies. Four emission cores of MF are resolved, in which two of them, MF1 and MF2, are connected to each other and located within the portion of the cloud with the low  $V_{\rm lsr}$  of  $\sim 64~{\rm km~s^{-1}}$ . For this velocity component, the distribution of MF is extended and offset

42 Xue et al.

from the continuum emission. The other two emission cores of MF, MF3 and MF4, with the high  $V_{\rm lsr}$ ,  $\sim 73~{\rm km~s^{-1}}$ , are separated by around 8.1" from each other. GLA also displays two velocity components, while the  $V_{\rm lsr}$  of GLA1 is  $\sim 64~{\rm km~s^{-1}}$  and of GLA2 is  $\sim 73~{\rm km~s^{-1}}$ . Only one velocity component of AcA, AcA1 at  $\sim 64~{\rm km~s^{-1}}$ , is resolved. In contrast to MF, the overall distribution of GLA and AcA are more compact and co-spatial with the continuum emission.

Because the distributions in the transition maps of each isomer are spatially consistent across a wide range of upper level energies, we rule out excitation conditions as the source of the distinct distributions of the  $C_2H_4O_2$  isomers. The dissimilar morphology of MF compared with GLA and AcA suggests that MF has a different formation mechanism than do GLA and AcA. Through a thorough investigation into the prevalent formation mechanisms involving both grain-surface and gas-phase routes, however, we find that the current existing chemical theory as summarized in Figure 16 can not explain the observed spatial distribution of the  $C_2H_4O_2$  isomers. In addition, different desorption behaviors of the three isomers could contribute to the spatial distributions of the  $C_2H_4O_2$  isomeric family. Therefore, more observations of the three isomers toward a larger sample of astronomical objects might help to constrain the morphological features and to probe the chemical formation mechanisms in these environments.

We acknowledge funding from the National Science Foundation for support of the astrochemistry program of E. H. Also special thanks go to K. H. Lam for helpful discussions on the quantification of the degree of consistency. We are indebted to B.A. McGuire for providing a Python program for simulating and visualizing molecular emission spectra, and to T. Hunter for providing codes to identify the continuum channels. A.M.B. was a Grote Reber Fellow for a portion of this project, and support for this work was provided by the NSF through the Grote Reber Fellowship Program administered by Associated Universities, Inc./National Radio Astronomy Observatory and the Virginia Space Grant Consortium. A.M.B. also acknowledges support from the Smithsonian Institution as a current Submillimeter Array (SMA) Fellow. This paper makes use of the following ALMA data: ADS/JAO.ALMA#2011.0.00017.S, ADS/JAO.ALMA#2012.1.00012.S. ALMA is a partner-

ship of ESO (representing its member states), NSF (USA) and NINS (Japan), together with NRC (Canada), NSC and ASIAA (Taiwan), and KASI (Republic of Korea), in cooperation with the Republic of Chile. The Joint ALMA Observatory is operated by ESO, AUI/NRAO and NAOJ.

Software: CASA (https://casa.nrao.edu) (Shaw et al. 2007)

44 Xue et al.

# **APPENDIX**

## A. COMPLEMENTARY TABLE

Tables 6, 7 and 8 list the transitions of the  $C_2H_4O_2$  isomers that are detected above the  $3\sigma$  level toward Sgr B2(N). P and D factors are calculated based on the observed spectra toward LMH and the simulated spectra assuming an excited temperature of 190 K. Comments in these tables acknowledge the reference observations.

**Table 6.** Transitions of MF with S/N > 3 covered by the EMoCA survey.

Rest Frequency	Transition	$E_u$	$\log_{10} \frac{A_{ul}}{\mathrm{s}^{-1}}$	$S_{ij}\mu^2$	P Factor	D Factor	Obs Ref
(MHz)		(K)		$(Debye^2)$	(%)	(%)	
84449.1690(100)	7(2,6) - 6(2,5)E	19.00	-5.0992	17.0	97.6	79.9	
84454.7540(100)	7(2,6) - 6(2,5)A	18.98	-5.0990	17.0	95.5	58.1	
85185.4660(100)	7(5,3) - 6(5,2)A v = 1	220.90	-5.3602	9.1	97.4	63.4	
85186.0630(100)	7(5,2) - 6(5,1)A v = 1	220.90	-5.3602	9.1	"	"	
85327.0290(100)	7(4,4) - 6(4,3)A v = 1	214.91	-5.2200	12.5	79.2	6.4	
85360.7640(100)	7(4,3) - 6(4,2)A v = 1	214.91	-5.2195	12.5	88.5	7.0	
85371.7300(100)	7(3,5) - 6(3,4)A v = 1	210.26	-5.1362	15.1	79.9	11.8	
85506.2190(100)	$7(4,3) - 6(4,2)E \ v = 1$	214.56	-5.2143	12.6	91.3	17.3	
85743.9760(100)	$7(4,4) - 6(4,3)E \ v = 1$	214.03	-5.2119	12.5	87.7	54.0	
85761.8760(100)	21(5,16) - 21(4,17)E	155.82	-5.8778	7.8	76.6	9.3	
85773.3990(100)	21(5,16) - 21(4,17)A	155.82	-5.8778	7.8	83.3	4.7	
85780.6730(100)	20(5,15) - 20(4,16)E	142.79	-5.8864	7.2	73.6	24.5	
85785.3420(100)	20(5,15) - 20(4,16)A	142.79	-5.8865	7.2	93.9	2.8	
85919.2090(100)	7(6,1) - 6(6,0)E	40.44	-5.6139	4.9	71.1	7.2	
85926.5530(100)	7(6,2) - 6(6,1)E	40.42	-5.6137	4.9	94.6	8.6	
85927.2270(100)	7(6,2) - 6(6,1)A	40.42	-5.6136	4.9	"	"	
85927.2270(100)	7(6,2) - 6(6,1)A	40.42	-5.6136	4.9	"	"	
86021.1240(100)	7(5,2) - 6(5,1)E	33.13	-5.3461	9.1	89.7	21.9	(Hollis et al. 2001)
86027.7230(100)	7(5,3) - 6(5,2)E	33.12	-5.3461	9.1	99.6	70.8	(Hollis et al. 2001)
86029.4420(100)	7(5,3) - 6(5,2)A	33.11	-5.3459	9.1	"	11	(Hollis et al. 2001)
86030.1860(100)	7(5,2) - 6(5,1)A	33.11	-5.3459	9.1	"	"	(Hollis et al. 2001)

Table 6 (continued)

Rest Frequency	Transition	$E_u$	$\log_{10} \frac{A_{ul}}{\mathrm{s}^{-1}}$	$S_{ij}\mu^2$	P Factor	D Factor	Obs Ref
(MHz)		(K)		$(Debye^2)$	(%)	(%)	
86034.0130(100)	$7(3,4) - 6(3,3)E \ v = 1$	209.82	-5.1231	15.2	97.5	34.6	
86155.0780(100)	7(3,4) - 6(3,3)A v = 1	210.32	-5.1242	15.1	92.2	12.8	
86172.7060(100)	$7(3,5) - 6(3,4)E \ v = 1$	209.41	-5.1242	15.1	99.3	23.7	
86210.0570(100)	7(4,4) - 6(4,3)A	27.15	-5.2050	12.5	84.7	23.3	
86223.6550(100)	7(4,3) - 6(4,2)E	27.17	-5.2074	12.5	99.3	65.2	
86224.1600(100)	7(4,4) - 6(4,3)E	27.16	-5.2075	12.5	"	"	
86250.5520(100)	7(4,3) - 6(4,2)A	27.15	-5.2044	12.5	91.0	33.0	(Hollis et al. 2001)
86265.7960(100)	7(3,5) - 6(3,4)A	22.51	-5.1210	15.2	99.7	63.2	(Hollis et al. 2001)
86268.7390(100)	7(3,5) - 6(3,4)E	22.53	-5.1248	15.1	99.7	69.3	(Hollis et al. 2001)
87143.2820(100)	7(3,4) - 6(3,3)E	22.60	-5.1116	15.1	95.1	51.1	
87160.8350(100)	$8(0,8) - 7(1,7)E \ v = 1$	207.04	-5.8948	2.8	99.2	33.9	
87161.2850(100)	7(3,4) - 6(3,3)A	22.58	-5.1074	15.2	"	"	
87766.3820(100)	8(0,8) - 7(1,7)E	20.08	-5.8757	2.9	98.7	19.6	
87960.0490(100)	7(1,6) - 6(1,5)A v = 1	205.65	-5.0223	18.0	93.9	11.5	
88053.9730(100)	19(5,14) - 19(4,15)E	130.44	-5.8713	6.6	99.4	31.3	
88054.4610(100)	19(5,14) - 19(4,15)A	130.44	-5.8716	6.6	"	"	
88220.7530(100)	$7(1,6) - 6(1,5)E \ v = 1$	204.91	-5.0168	18.1	93.9	12.3	
88337.8140(100)	22(5,17) - 22(4,18)E	169.52	-5.8423	8.1	70.6	4.0	
88358.4870(100)	22(5,17) - 22(4,18)A	169.52	-5.8422	8.1	99.4	28.7	
88770.8680(100)	8(1,8) - 7(1,7)A v = 1	207.91	-5.0025	20.8	97.9	32.1	
88843.1870(100)	7(1,6) - 6(1,5)E	17.96	-5.0081	18.0	89.1	25.0	
88851.6070(100)	7(1,6) - 6(1,5)A	17.94	-5.0079	18.0	95.0	35.8	
88998.3650(100)	7(2,5) - 6(2,4)A v = 1	207.37	-5.0298	17.1	97.4	40.9	
89140.3750(100)	$7(2,5) - 6(2,4)E \ v = 1$	206.70	-5.0277	17.1	96.2	6.2	
89314.6570(100)	8(1,8) - 7(1,7)E	20.15	-4.9931	20.8	99.2	15.2	
89316.6420(100)	8(1,8) - 7(1,7)A	20.14	-4.9929	20.8	100.0	8.1	
89731.6950(100)	8(0,8) - 7(0,7)A v = 1	207.83	-4.9870	20.8	91.8	10.1	
89829.7040(100)	$8(0,8) - 7(0,7)E \ v = 1$	207.04	-4.9832	20.9	98.4	21.9	
90145.7230(100)	7(2,5) - 6(2,4)E	19.68	-5.0114	17.1	99.8	25.4	(Remijan et al. 2003)
							(Requena-Torres et al. 2006
90156.4730(100)	7(2,5) - 6(2,4)A	19.67	-5.0111	17.1	98.7	28.2	(Remijan et al. 2003)
							(Requena-Torres et al. 2006

Table 6 continued on next page

XUE ET AL.

Table 6 (continued)

Rest Frequency	Transition	$E_u$	$\log_{10} \frac{A_{ul}}{\mathrm{s}^{-1}}$	$S_{ij}\mu^2$	P Factor	D Factor	Obs Ref
(MHz)		(K)		$(Debye^2)$	(%)	(%)	
90227.6590(100)	8(0,8) - 7(0,7)E	20.08	-4.9785	20.9	100.0	50.4	(Remijan et al. 2003)
							(Requena-Torres et al. 2006)
90229.6240(100)	8(0,8) - 7(0,7)A	20.06	-4.9783	20.9	99.5	45.1	(Remijan et al. 2003)
							(Requena-Torres et al. 2006)
91775.9350(100)	8(1,8) - 7(0,7)E	20.15	-5.8125	2.9	99.5	29.1	
91776.8860(100)	20(4,16) - 20(3,17)E	138.67	-5.8587	6.3	"	"	
91777.2300(100)	8(1,8) - 7(0,7)A	20.14	-5.8128	2.9	"	"	
92073.1010(100)	18(5,13) - 18(4,14)A	118.78	-5.8392	5.9	87.8	10.7	
92074.0200(100)	18(5,13) - 18(4,14)E	118.79	-5.8391	5.9	"	"	
95242.0050(100)	8(2,7) - 7(2,6)A v = 1	211.31	-4.9318	19.8	94.9	37.5	
95689.3990(100)	$8(2,7) - 7(2,6)E \ v = 1$	210.57	-4.9247	19.8	83.2	18.4	
96070.7250(100)	8(2,7) - 7(2,6)E	23.61	-4.9191	19.8	97.7	97.6	
96076.8450(100)	8(2,7) - 7(2,6)A	23.59	-4.9189	19.8	99.4	51.8	
97199.1110(100)	17(5,12) - 17(4,13)E	107.82	-5.7969	5.2	II.	"	
97199.2220(100)	17(5,12) - 17(4,13)A	107.81	-5.7970	5.2	II.	"	
97304.7110(100)	8(7,1) - 7(7,0)A v = 1	241.56	-5.5029	5.0	93.2	0.8	
97304.7110(100)	8(7,1) - 7(7,0)A v = 1	241.56	-5.5029	5.0	"	"	
97350.4170(300)	8(6,2) - 7(6,1)A v = 1	232.90	-5.2315	9.3	96.8	56.8	
97350.4170(300)	8(6,2) - 7(6,1)A v = 1	232.90	-5.2315	9.3	II.	"	
97395.3420(100)	$8(6,2) - 7(6,1)E \ v = 1$	232.82	-5.2291	9.3	94.3	15.3	
97457.9670(100)	8(5,4) - 7(5,3)A v = 1	225.57	-5.0864	12.9	89.1	17.6	
97460.3950(100)	8(5,3) - 7(5,2)A v = 1	225.57	-5.0863	12.9	93.3	26.3	
97577.3030(100)	$8(5,3) - 7(5,2)E \ v = 1$	225.36	-5.0824	13.0	72.9	43.2	
97597.1610(100)	8(3,6) - 7(3,5)A v = 1	214.94	-4.9360	18.2	79.2	14.5	
97651.2700(300)	10(4,7) - 10(3,8)E	43.17	-5.9016	2.4	80.6	10.1	
97651.2700(300)	10(4,7) - 10(3,8)E	43.17	-5.9016	2.4	"	"	
97661.4010(100)	8(4,5) - 7(4,4)A v = 1	219.60	-4.9937	15.9	93.4	24.8	
97738.7380(100)	$8(6,3) - 7(6,2)E \ v = 1$	232.09	-5.2243	9.3	"	"	
97752.8850(100)	8(4,4) - 7(4,3)A v = 1	219.60	-4.9924	15.9	80.4	58.4	
97885.6630(100)	$8(5,4) - 7(5,3)E \ v = 1$	224.73	-5.0787	13.0	91.4	20.6	
97897.1180(100)	$8(4,4) - 7(4,3)E \ v = 1$	219.26	-4.9875	16.0	99.3	42.5	
98176.2930(100)	$8(4,5) - 7(4,4)E \ v = 1$	218.74	-4.9853	16.0	82.3	1.8	

Table 6 (continued)

Rest Frequency	Transition	$E_u$	$\log_{10} \frac{A_{ul}}{\mathrm{s}^{-1}}$	$S_{ij}\mu^2$	P Factor	D Factor	Obs Ref
(MHz)		(K)		(Debye <sup>2</sup> )	(%)	(%)	
98182.3360(100)	8(7,1) - 7(7,0)E	53.78	-5.4902	5.0	80.2	2.7	
98190.6580(100)	8(7,2) - 7(7,1)A	53.76	-5.4900	5.0	99.7	34.8	
98190.6580(100)	8(7,2) - 7(7,1)A	53.76	-5.4900	5.0	"	"	
98191.4600(100)	8(7,2) - 7(7,1)E	53.76	-5.4901	5.0	"	11	
98270.5010(100)	8(6,2) - 7(6,1)E	45.15	-5.2180	9.3	79.0	15.2	
98278.9210(100)	8(6,3) - 7(6,2)E	45.13	-5.2179	9.3	96.4	65.3	
98279.7620(100)	8(6,3) - 7(6,2)A	45.13	-5.2178	9.3	"	"	
98279.7620(100)	8(6,3) - 7(6,2)A	45.13	-5.2178	9.3	"	11	
98423.1650(100)	9(0,9) - 8(1,8)A v = 1	212.63	-5.7011	3.4	91.4	36.1	
98424.2070(100)	8(5,3) - 7(5,2)E	37.86	-5.0722	13.0	"	11	
98431.8030(100)	8(5,4) - 7(5,3)E	37.84	-5.0721	13.0	98.9	38.8	
98432.7600(100)	8(5,4) - 7(5,3)A	37.84	-5.0720	13.0	"	"	
98435.8020(100)	8(5,3) - 7(5,2)A	37.84	-5.0720	13.0	99.7	33.3	
98606.8560(100)	8(3,6) - 7(3,5)E	27.26	-4.9216	18.2	82.3	9.4	
98611.1630(100)	8(3,6) - 7(3,5)A	27.24	-4.9209	18.3	97.9	4.0	
98682.4210(100)	8(3,6) - 7(3,5)E v = 1	214.15	-4.9245	18.1	99.7	54.8	
98682.6150(100)	8(4,5) - 7(4,4)A	31.89	-4.9786	16.0	"	11	
98712.0010(100)	8(4,5) - 7(4,4)E	31.90	-4.9928	15.4	89.5	6.6	
98713.6550(100)	26(8,18) - 25(9,17)E	250.95	-6.7530	0.8	"	11	
98747.9060(100)	8(4,4) - 7(4,3)E	31.91	-4.9923	15.4	93.0	8.8	
98792.2890(100)	8(4,4) - 7(4,3)A	31.89	-4.9772	16.0	91.5	11.1	
98815.2900(100)	8(3,5) - 7(3,4)E v = 1	214.56	-4.9193	18.2	95.6	36.2	
99089.5180(100)	8(3,5) - 7(3,4)A v = 1	215.08	-4.9159	18.2	98.7	64.8	
99133.2720(100)	9(0,9) - 8(1,8)E	24.91	-5.6979	3.4	98.8	22.3	
99135.7620(100)	9(0,9) - 8(1,8)A	24.89	-5.6982	3.4	100.0	13.0	
99489.0570(100)	9(1,9) - 8(1,8)A v = 1	212.69	-4.8499	23.4	99.1	39.4	
99575.5480(100)	8(1,7) - 7(1,6)A v = 1	210.43	-4.8565	20.6	98.1	31.1	
99577.4190(100)	$9(1,9) - 8(1,8)E \ v = 1$	211.90	-4.8461	23.6	"	"	
99869.1020(100)	$8(1,7) - 7(1,6)E \ v = 1$	209.71	-4.8509	20.7	94.0	10.4	
100078.6080(100)	9(1,9) - 8(1,8)E	24.96	-4.8407	23.5	96.9	9.7	
100080.5420(100)	9(1,9) - 8(1,8)A	24.94	-4.8406	23.5	94.7	6.8	
100136.9130(100)	9(0,9) - 8(0,8)A v = 1	212.63	-4.8407	23.5	73.1	13.2	

Xue et al.

Table 6 (continued)

Rest Frequency	Transition	$E_u$	$\log_{10} \frac{A_{ul}}{\mathrm{s}^{-1}}$	$S_{ij}\mu^2$	P Factor	D Factor	Obs Ref
(MHz)		(K)		$(Debye^2)$	(%)	(%)	
100226.6840(100)	$9(0,9) - 8(0,8)E \ v = 1$	211.85	-4.8370	23.6	81.9	31.9	
100294.6040(100)	8(3,5) - 7(3,4)E	27.41	-4.8992	18.3	99.7	32.3	
100308.1790(100)	8(3,5) - 7(3,4)A	27.40	-4.8985	18.3	99.3	37.7	
100482.2410(100)	8(1,7) - 7(1,6)E	22.78	-4.8437	20.6	99.8	13.5	
100490.6820(100)	8(1,7) - 7(1,6)A	22.76	-4.8435	20.6	87.5	20.6	
100681.5450(100)	9(0,9) - 8(0,8)E	24.91	-4.8323	23.5	98.2	34.9	
100683.3680(100)	9(0,9) - 8(0,8)A	24.89	-4.8322	23.5	"	"	
101626.8840(100)	9(1,9) - 8(0,8)E	24.96	-5.6633	3.4	90.9	24.9	
101628.1490(100)	9(1,9) - 8(0,8)A	24.94	-5.6636	3.4	"	"	
102179.5100(100)	8(2,6) - 7(2,5)A v = 1	212.27	-4.8370	19.9	96.5	8.8	
102503.1050(100)	8(2,6) - 7(2,5)E v = 1	211.62	-4.8307	20.0	92.3	25.2	
102734.2120(100)	16(5,11) - 16(4,12)E	97.52	-5.7520	4.6	99.6	18.0	
102736.8690(100)	16(5,11) - 16(4,12)A	97.51	-5.7519	4.6	99.3	16.2	
103376.8420(100)	24(6,18) - 24(5,19)A	203.82	-5.6555	8.4	70.8	11.7	
103387.2000(100)	24(6,18) - 24(5,19)E	203.82	-5.6553	8.4	91.0	2.5	
103466.5720(100)	8(2,6) - 7(2,5)E	24.65	-4.8190	20.0	98.3	42.2	
103478.6630(100)	8(2,6) - 7(2,5)A	24.63	-4.8187	20.0	98.9	63.4	
106648.7540(100)	9(2,8) - 8(2,7)A v = 1	216.42	-4.7760	22.5	95.6	8.8	
107022.1590(100)	$9(2,8) - 8(2,7)E \ v = 1$	215.71	-4.7693	22.6	79.3	6.5	
107537.2580(100)	9(2,8) - 8(2,7)E	28.77	-4.7639	22.6	75.8	20.4	(Remijan et al. 2003)
107543.7110(100)	9(2,8) - 8(2,7)A	28.75	-4.7637	22.6	98.3	5.9	(Remijan et al. 2003)
107590.3890(100)	23(6,17) - 23(5,18)A	189.04	-5.6251	7.7	91.8	1.0	
107604.3660(100)	23(6,17) - 23(5,18)E	189.04	-5.6248	7.7	93.9	1.1	
108045.9590(100)	15(5,10) - 15(4,11)E	87.87	-5.7107	4.1	94.6	25.3	
108050.9390(100)	15(5,10) - 15(4,11)A	87.86	-5.7099	4.1	88.1	25.4	
109501.2460(100)	9(8,1) - 8(8,0)A v = 1	256.83	-5.3939	5.0	84.9	2.5	
109501.2460(100)	9(8,1) - 8(8,0)A v = 1	256.83	-5.3939	5.0	"	"	
109502.6550(100)	$9(7,2) - 8(7,1)E \ v = 1$	246.89	-5.1181	9.5	"	"	
109531.4130(100)	9(7,2) - 8(7,1)A v = 1	246.82	-5.1190	9.4	99.5	34.9	
109531.4130(100)	9(7,2) - 8(7,1)A v = 1	246.82	-5.1190	9.4	11	"	
109608.5400(300)	9(6,3) - 8(6,2)A v = 1	238.16	-4.9703	13.3	64.0	11.3	
109608.5400(300)	9(6,3) - 8(6,2)A v = 1	238.16	-4.9703	13.3	"	"	

Table 6 (continued)

Rest Frequency	Transition	$E_u$	$\log_{10} \frac{A_{ul}}{\mathrm{s}^{-1}}$	$S_{ij}\mu^2$	P Factor	D Factor	Obs Ref
(MHz)		(K)		$(Debye^2)$	(%)	(%)	
109662.9440(100)	$9(6,3) - 8(6,2)E \ v = 1$	238.08	-4.9679	13.3	90.5	66.7	
109763.7370(100)	9(3,7) - 8(3,6)A v = 1	220.21	-4.7655	21.2	91.3	12.2	
109770.9950(100)	9(5,5) - 8(5,4)A v = 1	230.84	-4.8736	16.5	89.0	11.5	
109778.8350(100)	9(5,4) - 8(5,3)A v = 1	230.84	-4.8735	16.5	94.7	3.0	
109912.1680(100)	9(5,4) - 8(5,3)E v = 1	230.63	-4.8697	16.6	80.5	3.2	
109924.8170(100)	$9(7,3) - 8(7,2)E \ v = 1$	246.10	-5.1124	9.5	87.8	70.9	
110035.2690(100)	9(4,6) - 8(4,5)A v = 1	224.88	-4.8060	19.2	97.6	7.2	
110050.3320(100)	$9(6,4) - 8(6,3)E \ v = 1$	237.38	-4.9631	13.3	96.4	1.8	
110153.6520(100)	10(1,10) - 9(1,9)A v = 1	217.97	-4.7139	26.1	94.6	14.8	
110364.5200(100)	$9(4,5) - 8(4,4)E \ v = 1$	224.55	-4.7991	19.3	99.4	2.6	
110447.1800(100)	9(8,1) - 8(8,0)E	69.04	-5.3818	5.0	93.3	6.3	
110455.3720(100)	9(8,2) - 8(8,1)A	69.03	-5.3817	5.0	89.4	43.3	
110455.3720(100)	9(8,2) - 8(8,1)A	69.03	-5.3817	5.0	"	"	
110458.0140(100)	9(8,2) - 8(8,1)E	69.02	-5.3817	5.0	11	"	
110525.7410(100)	9(7,2) - 8(7,1)E	59.09	-5.1063	9.5	83.0	60.7	
110526.1900(100)	$7(2,6) - 6(1,5)A \ v = 1$	206.74	-5.8286	1.4	11	"	
110535.1860(100)	9(7,3) - 8(7,2)A	59.07	-5.1061	9.5	91.3	67.5	
110535.1860(100)	9(7,3) - 8(7,2)A	59.07	-5.1061	9.5	"	"	
110536.0030(100)	9(7,3) - 8(7,2)E	59.07	-5.1061	9.5	11	"	
110571.6320(100)	10(0,10) - 9(0,9)A v = 1	217.94	-4.7086	26.1	93.4	28.8	
110652.8130(100)	9(6,3) - 8(6,2)E	50.46	-4.9568	13.3	98.5	30.4	
110655.3100(100)	$10(0,10) - 9(0,9)E \ v = 1$	217.16	-4.7051	26.3	98.6	16.3	
110662.3150(100)	9(6,4) - 8(6,3)E	50.45	-4.9567	13.3	77.1	19.0	
110663.2730(100)	9(6,4) - 8(6,3)A	50.44	-4.9566	13.3	"	"	
110663.4290(100)	9(6,3) - 8(6,2)A	50.44	-4.9566	13.3	"	"	
110684.1230(100)	$9(4,6) - 8(4,5)E \ v = 1$	224.06	-4.7970	19.2	92.6	2.9	
110776.4990(100)	9(1,8) - 8(1,7)A v = 1	215.75	-4.7150	23.1	96.9	68.0	
110788.6640(100)	10(1,10) - 9(1,9)E	30.27	-4.7051	26.2	96.6	62.5	
110790.5260(100)	10(1,10) - 9(1,9)A	30.26	-4.7049	26.2	"	"	
110873.9550(100)	9(5,4) - 8(5,3)E	43.18	-4.8594	16.6	96.8	57.9	
110879.7660(100)	9(3,7) - 8(3,6)E	32.58	-4.7510	21.2	97.1	89.6	
110880.4470(100)	9(5,5) - 8(5,4)A	43.16	-4.8592	16.6	"	"	

Table 6 (continued)

Rest Frequency	Transition	$E_u$	$\log_{10} \frac{A_{ul}}{s^{-1}}$	$S_{ij}\mu^2$	P Factor	D Factor	Obs Ref
(MHz)		(K)		$(Debye^2)$	(%)	(%)	
110882.3310(100)	9(5,5) - 8(5,4)E	43.16	-4.8594	16.6	"	"	
110887.0920(100)	9(3,7) - 8(3,6)A	32.57	-4.7507	21.3	99.8	52.7	
110890.2560(100)	9(5,4) - 8(5,3)A	43.16	-4.8590	16.6	99.4	39.2	
111005.6720(100)	$9(3,7) - 8(3,6)E \ v = 1$	219.48	-4.7583	20.8	70.7	13.4	
111094.1240(100)	$9(1,8) - 8(1,7)E \ v = 1$	215.04	-4.7094	23.2	71.8	14.7	
111169.9030(100)	10(0,10) - 9(0,9)E	30.25	-4.7002	26.2	99.6	82.7	
111171.6340(100)	10(0,10) - 9(0,9)A	30.23	-4.7001	26.2	"	"	
111195.9620(100)	9(4,6) - 8(4,5)A	37.22	-4.7909	19.2	93.9	55.9	
111223.4910(100)	9(4,6) - 8(4,5)E	37.23	-4.8145	18.2	98.7	53.0	
111224.9860(100)	14(3,11) - 13(4,10)E v = 1	256.70	-6.3187	0.9	"	"	
111408.4120(100)	9(4,5) - 8(4,4)E	37.26	-4.8123	18.2	94.9	86.1	(Requena-Torres et al. 2006)
111453.3000(100)	9(4,5) - 8(4,4)A	37.24	-4.7878	19.2	99.9	75.0	(Remijan et al. 2003)
111674.1310(100)	9(1,8) - 8(1,7)E	28.14	-4.7037	23.2	99.6	78.7	(Requena-Torres et al. 2006)
111682.1890(100)	9(1,8) - 8(1,7)A	28.12	-4.7035	23.2	99.6	58.9	(Requena-Torres et al. 2006)
111734.0020(100)	10(1,10) - 9(0,9)E	30.27	-5.5269	3.8	95.9	36.0	
111735.3070(100)	10(1,10) - 9(0,9)A	30.26	-5.5271	3.8	"	"	
112011.9660(100)	9(3,6) - 8(3,5)E v = 1	219.94	-4.7426	21.0	"	"	
112306.9410(100)	9(3,6) - 8(3,5)A v = 1	220.47	-4.7352	21.2	96.7	18.8	
113743.1070(100)	9(3,6) - 8(3,5)E	32.87	-4.7171	21.3	98.1	14.4	
113756.6100(100)	9(3,6) - 8(3,5)A	32.86	-4.7168	21.3	99.1	30.5	

Note—Pertinent parameters of the detected transitions of MF taken from JPL catalog. The transitions with ditto marks in the column of P and D factors are blended with the transitions in the previous row.

**Table 7**. Transitions of GLA with S/N > 3 covered by the EMoCA survey.

Rest Frequency	Transition	$E_u$	$\log_{10} \frac{A_{ul}}{s^{-1}}$	$S_{ij}\mu^2$	P Factor	D Factor	Obs Ref
(MHz)		(K)		$(\text{Debye}^2)$	(%)	(%)	
85288.3467(47)	8(4,4) - 8(3,5)	29.74	-5.0287	22.0	73.0	63.8	
85476.6666(92)	11(1,10) - 11(0,11)	37.91	-5.3021	15.8	97.9	41.4	
85782.2440(55)	8(1,8) - 7(0,7)	18.87	-4.8264	34.5	73.6	31.2	(Halfen et al. 2006)

Table 7 (continued)

Rest Frequency	Transition	$E_u$	$\log_{10} \frac{A_{ul}}{\mathrm{s}^{-1}}$	$S_{ij}\mu^2$	P Factor	D Factor	Obs Ref
(MHz)		(K)		$(Debye^2)$	(%)	(%)	
86600.5997(67)	17(5,12) - 17(4,13)	101.14	-4.8624	63.6	91.0	86.6	
87764.5007(47)	5(2,4) - 4(1,3)	10.69	-5.0665	12.0	84.5	27.8	
87812.2080(47)	6(4,2) - 6(3,3)	21.38	-5.0745	13.9	94.3	8.9	
88425.7474(47)	7(4,4) - 7(3,5)	25.27	-5.0198	17.8	99.0	20.7	
88463.7084(47)	6(4,3) - 6(3,4)	21.38	-5.0662	13.9	90.7	15.9	
88530.4001(46)	8(4,5) - 8(3,6)	29.73	-4.9874	21.7	94.9	68.9	
88691.2605(68)	12(3,10) - 12(2,11)	48.77	-5.0203	29.4	92.2	58.9	
88892.4467(45)	9(4,6) - 9(3,7)	34.76	-4.9607	25.4	85.0	14.1	
89616.3982(132)	20(4,16) - 20(3,17)	130.44	-4.8374	71.2	98.4	29.8	
89644.1477(45)	10(4,7) - 10(3,8)	40.35	-4.9352	29.1	89.7	2.2	
89832.2856(115)	14(2,12) - 14(1,13)	62.93	-5.0296	32.1	91.8	39.5	
89868.6318(54)	9(1,8) - 8(2,7)	26.42	-5.0389	20.6	94.0	16.8	(Halfen et al. 2006)
90187.0697(109)	23(5,18) - 23(4,19)	172.97	-4.7716	93.1	95.7	28.2	
90507.2610(133)	17(3,14) - 17(2,15)	93.78	-4.9064	50.3	98.1	80.4	
90591.3442(78)	11(2,10) - 11(1,11)	38.17	-5.2329	15.5	86.6	1.8	
90922.2144(46)	11(4,8) - 11(3,9)	46.51	-4.9075	32.5	58.2	22.1	
91712.9604(71)	16(5,11) - 16(4,12)	91.41	-4.8169	56.0	74.2	7.9	
92738.2867(52)	25(6,19) - 25(5,20)	206.18	-4.7044	108.5	85.7	27.2	
92853.9487(49)	12(4,9) - 12(3,10)	53.23	-4.8762	35.7	97.2	79.2	
93048.5007(46)	24(6,18) - 24(5,19)	191.55	-4.7088	102.2	94.2	27.1	
93052.6745(56)	9(0,9) - 8(1,8)	23.34	-4.7062	39.8	95.7	44.1	(Hollis et al. 2000)
							(Halfen et al. 2006)
95070.0983(60)	9(1,9) - 8(0,8)	23.37	-4.6763	40.0	78.9	10.5	(Halfen et al. 2006)
95175.1800(76)	26(6,20) - 26(5,21)	221.45	-4.6731	112.1	84.4	31.5	
95300.4082(75)	13(3,11) - 13(2,12)	55.93	-4.9488	30.2	84.9	26.7	
95443.0896(53)	6(2,5) - 5(1,4)	13.97	-4.9612	14.0	99.5	1.2	
95544.7538(53)	13(4,10) - 13(3,11)	60.52	-4.8397	38.5	82.6	18.2	
95741.7260(94)	12(1,11) - 12(0,12)	44.35	-5.1911	15.8	79.9	4.6	
95756.2369(57)	23(6,17) - 23(5,18)	177.57	-4.6897	94.0	83.9	58.9	
96078.4307(75)	11(2,9) - 10(3,8)	40.66	-5.1981	14.1	75.8	13.6	
96870.7828(70)	15(5,10) - 15(4,11)	82.31	-4.7720	49.5	89.6	67.1	
97919.5791(49)	3(3,1) - 2(2,0)	8.80	-4.6806	13.4	7.1	49.1	

Table 7 continued on next page

XUE ET AL.

Table 7 (continued)

Rest Frequency	Transition	$E_u$	$\log_{10} \frac{A_{ul}}{\mathrm{s}^{-1}}$	$S_{ij}\mu^2$	P Factor	D Factor	Obs Ref
(MHz)		(K)		$(Debye^2)$	(%)	(%)	
98070.5113(49)	3(3,0) - 2(2,1)	8.80	-4.6793	13.3	87.8	12.2	
99068.4727(59)	14(4,11) - 14(3,12)	68.36	-4.7976	40.8	71.4	20.6	
99109.9990(83)	12(2,11) - 12(1,12)	44.52	-5.1491	15.7	99.6	41.8	
99346.4488(133)	24(5,19) - 24(4,20)	187.08	-4.6741	90.9	93.1	11.8	
100323.8733(73)	22(6,16) - 22(5,17)	164.25	-4.6532	85.1	92.8	2.2	
100506.6546(103)	27(6,21) - 27(5,22)	237.35	-4.6155	112.8	92.7	21.8	
101116.3124(145)	21(4,17) - 21(3,18)	142.69	-4.7161	68.7	99.6	39.5	
101232.1720(115)	15(2,13) - 15(1,14)	71.31	-4.9076	31.8	79.8	21.7	
101527.8515(65)	14(5,9) - 14(4,10)	73.82	-4.7334	44.0	93.9	15.0	
102549.7240(60)	7(2,6) - 6(1,5)	17.78	-4.8570	16.6	76.3	8.1	(Halfen et al. 2006)
102572.9391(82)	14(3,12) - 14(2,13)	63.60	-4.8764	30.7	99.0	62.2	
102614.3429(137)	18(3,15) - 18(2,16)	104.10	-4.7784	49.0	97.9	64.4	
103391.2854(62)	10(0,10) - 9(1,9)	28.34	-4.5552	45.5	93.5	26.3	(Hollis et al. 2000)
							(Halfen et al. 2006)
103461.3106(66)	15(4,12) - 15(3,13)	76.75	-4.7501	42.8	95.0	77.7	
103667.9094(57)	10(1,9) - 9(2,8)	31.93	-4.7910	26.2	91.3	58.6	(Hollis et al. 2000)
							(Halfen et al. 2006)
104587.7032(64)	10(1,10) - 9(0,9)	28.36	-4.5394	45.5	88.2	6.9	(Halfen et al. 2006)
105355.6639(59)	13(5,8) - 13(4,9)	65.93	-4.7051	39.1	99.2	16.0	
106067.4262(84)	21(6,15) - 21(5,16)	151.60	-4.6068	76.6	87.7	21.6	
106710.9951(60)	29(7,22) - 29(6,23)	275.99	-4.5255	124.4	87.1	22.4	
107380.1425(74)	30(7,23) - 30(6,24)	293.59	-4.5135	129.8	81.9	21.5	
107663.7353(115)	19(5,14) - 18(6,13)	122.53	-5.3224	12.8	88.9	13.9	
107874.8614(87)	13(2,12) - 13(1,13)	51.36	-5.0703	15.7	99.4	13.3	
108261.4557(56)	12(5,7) - 12(4,8)	58.63	-4.6885	34.7	94.7	40.1	
108719.6747(73)	16(4,13) - 16(3,14)	85.69	-4.6979	44.2	94.6	3.8	
108824.4021(62)	28(7,21) - 28(6,22)	259.05	-4.5133	116.5	98.2	59.3	
109114.1722(53)	4(3,2) - 3(2,1)	11.02	-4.6411	13.6	79.0	18.3	
109280.0092(66)	8(2,7) - 7(1,6)	22.11	-4.7522	19.8	87.7	60.2	(Halfen et al. 2006)
109877.1408(54)	4(3,1) - 3(2,2)	11.02	-4.6354	13.5	77.9	1.9	
110330.6028(55)	11(5,6) - 11(4,7)	51.91	-4.6836	30.5	99.2	3.3	
110402.5367(87)	15(3,13) - 15(2,14)	71.79	-4.8048	31.0	99.4	80.3	

Table 7 continued on next page

Table 7 (continued)

Rest Frequency	Transition	$E_u$	$\log_{10} \frac{A_{ul}}{\mathrm{s}^{-1}}$	$S_{ij}\mu^2$	P Factor	D Factor	Obs Ref
(MHz)		(K)		$(Debye^2)$	(%)	(%)	
110608.5089(148)	25(5,20) - 25(4,21)	201.73	-4.5659	88.0	84.5	3.9	
110845.1604(102)	14(3,11) - 13(4,10)	65.84	-5.1366	13.4	74.9	2.8	
111098.2681(97)	31(7,24) - 31(6,25)	311.83	-4.4755	132.1	97.6	53.3	
111734.8569(55)	10(5,5) - 10(4,6)	45.76	-4.6897	26.4	98.5	47.0	
112177.7128(51)	13(5,9) - 13(4,10)	65.90	-4.6338	38.2	75.4	27.1	
112210.4422(52)	12(5,8) - 12(4,9)	58.62	-4.6471	34.3	92.2	70.7	
112247.9894(87)	20(6,14) - 20(5,15)	139.58	-4.5575	69.0	81.7	25.9	
112341.6773(114)	16(2,14) - 16(1,15)	80.14	-4.8011	31.6	94.4	22.8	
112444.3079(53)	11(5,7) - 11(4,8)	51.90	-4.6614	30.3	86.6	31.1	
112472.7946(50)	14(5,10) - 14(4,11)	73.76	-4.6197	42.0	98.6	98.4	
112656.0535(56)	9(5,4) - 9(4,5)	40.19	-4.7071	22.4	69.6	8.7	
112773.4455(55)	10(5,6) - 10(4,7)	45.76	-4.6788	26.4	81.6	9.2	
113326.8996(77)	12(2,10) - 11(3,9)	47.58	-4.9081	18.2	88.5	14.4	(Halfen et al. 2006)
113429.3652(57)	8(5,4) - 8(4,5)	35.18	-4.7360	18.4	95.7	5.9	
113569.5317(66)	11(0,11) - 10(1,10)	33.81	-4.4222	51.0	75.3	42.3	(Halfen et al. 2006)
113616.7028(57)	7(5,2) - 7(4,3)	30.73	-4.7891	14.3	83.5	5.3	
113679.1292(57)	7(5,3) - 7(4,4)	30.73	-4.7884	14.3	95.8	7.9	
113694.9880(150)	22(4,18) - 22(3,19)	155.43	-4.5962	66.7	95.6	10.1	
114264.4356(67)	11(1,11) - 10(0,10)	33.82	-4.4139	51.1	95.8	29.3	(Halfen et al. 2006)

Note—Pertinent parameters of the detected transitions of GLA taken from CDMS catalog. The transitions with ditto marks in the column of P and D factors are blended with the transitions in the previous row.

**Table 8.** Transitions of AcA with S/N > 3 covered by the EMoCA survey.

Rest Frequency (MHz)	Transition	$E_u$ (K)	$\log_{10} \frac{A_{ul}}{s^{-1}}$	$S_{ij}\mu^2$ (Debye <sup>2</sup> )	P Factor (%)	D Factor (%)	Obs Ref
84857.3100(10)	10(2,8) - 10(2,9) + -	39.18	-6.4449	1.1	89.4	62.3	
84857.3200(10)	10(2,8) - 10(1,9) + -	39.18	-5.7818	4.9	"	II	
84857.8300(10)	10(3,8) - 10(2,9) + -	39.18	-5.7818	4.9	"	II	
84857.8300(10)	10(3,8) - 10(2,9) + -	39.18	-5.7818	4.9	11	II .	

XUE ET AL.

Table 8 (continued)

Rest Frequency	Transition	$E_u$	$\log_{10} \frac{A_{ul}}{\mathrm{s}^{-1}}$	$S_{ij}\mu^2$	P Factor	D Factor	Obs Ref
(MHz)		(K)		$(\text{Debye}^2)$	(%)	(%)	
85399.0300(10)	19(10,9) - 19(9,10) + -	167.72	-5.3809	22.4	89.8	50.3	
85981.5900(10)	19(-10,9) - 19(-9,10)	167.84	-5.3722	22.4	81.1	22.7	
86473.4400(20)	23(15,9) - 23(14,10) + -	251.63	-5.3148	30.2	95.1	4.7	
86569.9100(10)	20(12,9) - 20(11,10) - +	187.34	-5.3465	24.4	80.8	86.5	
86879.0100(20)	23(13,10) - 23(12,11) - +	247.08	-5.3194	29.5	96.5	6.0	
87631.1000(40)	15(-11,4) - 15(-9,6)	113.06	-7.0292	0.4	95.5	5.6	
87632.9100(10)	19(11,9) - 19(10,10)	167.92	-5.3486	22.3	"	"	
87759.3100(30)	14(-14,0) - 14(-13,1)	112.51	-5.9766	3.9	91.1	14.8	
87761.2200(10)	19(11,9) - 19(10,10) + -	167.84	-5.3475	22.3	"	"	
87822.7200(10)	4(-4,0) - 3(-3,0)	10.91	-5.2581	6.3	84.7	3.6	
87823.6800(10)	6(2,4) - 5(3,3) + +	16.93	-5.4130	6.4	"	"	
89516.9600(10)	7(-1,6) - 6(2,5)	19.59	-5.1941	11.5	93.2	9.2	
89518.9500(10)	7(2,6) - 6(2,5)	19.59	-5.6395	4.1	"	"	
89531.1900(10)	7(-1,6) - 6(-1,5)	19.59	-5.6393	4.1	88.9	55.7	
89533.1800(10)	7(2,6) - 6(-1,5)	19.59	-5.1939	11.5	"	"	
89653.2800(10)	7(1,6) - 6(2,5)	19.12	-5.1974	11.3	92.7	3.4	
89677.4100(10)	7(2,6) - 6(1,5)	19.12	-5.1971	11.3	90.3	3.2	
90203.4400(10)	8(*,8) - 7(1,7)	20.83	-4.9646	21.6	99.0	23.3	(Mehringer et al. 1997)
							(Remijan et al. 2003)
90203.4600(10)	8(*,8) - 7(0,7)	20.83	-4.9646	21.6	"	"	(Mehringer et al. 1997)
							(Remijan et al. 2003)
90246.2400(10)	8(*,8) - 7(1,7) + +	20.33	-4.9642	21.6	96.8	47.1	(Mehringer et al. 1997)
							(Remijan et al. 2003)
90246.2700(10)	8(*,8) - 7(0,7) + +	20.33	-4.9642	21.6	"	"	(Mehringer et al. 1997)
							(Remijan et al. 2003)
93760.4300(10)	12(-3,9) - 12(*,10)	58.24	-5.4784	8.7	66.9	16.1	
93760.6900(10)	12(4,9) - 12(3,10)	58.24	-5.5568	7.2	"	"	
93760.6900(10)	12(4,9) - 12(3,10)	58.24	-5.5568	7.2	"	"	
94499.3200(10)	12(3,9) - 12(3,10) - +	57.87	-6.2182	1.5	76.9	33.9	
94499.3300(10)	12(3,9) - 12(2,10) - +	57.87	-5.5502	7.2	"	"	
94499.8200(10)	12(4,9) - 12(3,10) - +	57.87	-5.5502	7.2	11	"	
94499.8300(10)	12(4,9) - 12(2,10) - +	57.87	-6.2182	1.5	11	11	

Table 8 (continued)

Rest Frequency	Transition	$E_u$	$\log_{10} \frac{A_{ul}}{\mathrm{s}^{-1}}$	$S_{ij}\mu^2$	P Factor	D Factor	Obs Ref
(MHz)		(K)		$(Debye^2)$	(%)	(%)	
95199.7500(10)	22(13,10) - 22(12,11)	225.12	-5.2227	26.8	75.9	1.8	
95243.0100(10)	22(13,10) - 22(12,11) + -	225.11	-5.2236	26.7	84.1	18.5	
95568.4100(10)	21(-11, 10) - 21(-10, 11)	203.65	-5.2349	24.6	72.9	23.6	
96694.7700(10)	21(12,10) - 21(11,11)	203.71	-5.2204	24.6	98.5	19.2	
96707.2300(10)	21(12,10) - 21(11,11) - +	203.68	-5.2216	24.5	80.5	17.0	
97347.3100(20)	25(14,11) - 25(13,12) + -	290.34	-5.1772	31.6	82.6	37.2	
97508.8900(10)	20(10,10) - 20(9,11) + -	183.14	-5.2308	22.3	72.8	22.7	
97685.6600(10)	20(-10, 10) - 20(-9, 11)	183.22	-5.2269	22.4	70.2	20.6	
98134.2400(10)	20(11,10) - 20(10,11)	183.25	-5.2211	22.4	96.5	4.3	
98194.4400(10)	20(11,10) - 20(10,11) + -	183.18	-5.2221	22.3	96.0	13.6	
99262.3700(10)	19(-9,10) - 19(-8,11)	163.72	-5.2288	20.2	98.6	27.4	
99341.5700(10)	7(-2,5) - 6(3,4)	22.19	-5.1689	8.9	80.3	18.1	
99424.7200(10)	7(3,5) - 6(3,4)	22.20	-5.5518	3.7	77.5	67.2	
99425.9200(10)	19(10, 10) - 19(9, 11)	163.73	-5.2266	20.2	"	"	
99487.5000(10)	7(2,5) - 6(3,4) + +	21.74	-5.1743	8.8	86.7	15.5	
99579.4600(10)	19(10,10) - 19(9,11) - +	163.63	-5.2268	20.1	65.9	12.3	
99862.2800(10)	7(3,5) - 6(-2,4)	22.19	-5.1601	8.9	79.9	13.5	
100168.7100(10)	8(-1,7) - 7(2,6)	24.40	-5.0256	13.7	100.0	10.4	
100168.9700(10)	8(2,7) - 7(2,6)	24.40	-5.4811	4.8	"	"	
100170.7000(10)	8(-1,7) - 7(-1,6)	24.40	-5.4810	4.8	99.8	18.4	
100170.9600(10)	8(2,7) - 7(-1,6)	24.40	-5.0256	13.7	"	"	
100202.9200(10)	7(3,5) - 6(2,4) + +	21.74	-5.1625	8.8	92.4	13.2	
100306.5300(10)	8(1,7) - 7(2,6)	23.94	-5.0295	13.5	87.4	23.4	
100306.9800(10)	8(2,7) - 7(2,6)	23.94	-5.4650	5.0	"	"	
100309.1100(40)	14(11,4) - 14(9,5) + -	100.77	-6.8014	0.4	92.0	15.3	
100309.6900(10)	8(1,7) - 7(1,6)	23.94	-5.4650	5.0	"	"	
100310.1300(10)	8(2,7) - 7(1,6)	23.94	-5.0295	13.5	"	"	
100481.8000(10)	18(-8,10) - 18(-7,11)	145.13	-5.2386	18.1	96.9	2.1	
100536.1900(10)	18(9,10) - 18(8,11)	145.15	-5.2378	18.1	73.8	40.3	
100855.4300(10)	9(*,9) - 8(*,8)	25.67	-4.5117	49.0	94.7	70.7	(Mehringer et al. 1997)
							(Remijan et al. 2003)
100897.4500(10)	9(*,9) - 8(*,8) + +	25.17	-4.5113	49.0	92.0	40.8	(Mehringer et al. 1997)

Table 8 continued on next page

XUE ET AL.

Table 8 (continued)

Rest Frequency	Transition	$E_u$	$\log_{10} \frac{A_{ul}}{\mathrm{s}^{-1}}$	$S_{ij}\mu^2$	P Factor	D Factor	Obs Ref
(MHz)		(K)		(Debye <sup>2</sup> )	(%)	(%)	
							(Remijan et al. 2003)
101448.7200(10)	17(-7,10) - 17(7,11)	127.51	-6.0030	2.9	65.9	10.4	
101449.4900(10)	17(-7,10) - 17(-6,11)	127.51	-5.2563	16.0	"	"	
101465.8700(10)	17(8,10) - 17(7,11)	127.51	-5.2561	16.0	80.3	49.9	
101466.6400(10)	17(8,10) - 17(-6,11)	127.51	-6.0028	2.9	"	"	
102227.0100(10)	16(-6,10) - 16(6,11)	110.83	-6.0173	2.5	90.0	2.1	
102227.1700(10)	16(-6,10) - 16(-5,11)	110.83	-5.2827	13.8	"	"	
102231.5800(10)	16(7,10) - 16(6,11)	110.83	-5.2827	13.8	73.9	4.6	
102231.7500(10)	16(7,10) - 16(-5,11)	110.83	-6.0173	2.5	"	II.	
102728.0300(10)	16(6,10) - 16(6,11) + -	110.62	-5.9798	2.7	93.9	23.0	
102728.3900(10)	16(6,10) - 16(5,11) + -	110.62	-5.2801	13.7	II.	"	
102736.4900(10)	16(7,10) - 16(6,11) + -	110.62	-5.2800	13.7	97.0	13.6	
102736.8400(10)	16(7,10) - 16(5,11) + -	110.62	-5.9796	2.7	II .	ıı	
102853.7400(10)	15(-5,10) - 15(5,11)	95.10	-6.0463	2.2	94.8	54.1	
102853.7700(10)	15(-5,10) - 15(-4,11)	95.10	-5.3206	11.7	"	II.	
102854.8100(10)	15(6,10) - 15(5,11)	95.10	-5.3206	11.7	"	ıı	
102854.8400(10)	15(6,10) - 15(-4,11)	95.10	-6.0463	2.2	"	II.	
103356.4500(10)	14(-4,10) - 14(4,11)	80.35	-6.0910	1.8	94.6	21.3	
103356.4600(10)	14(-4,10) - 14(-3,11)	80.35	-5.3743	9.5	"	ıı	
103356.6700(10)	14(5,10) - 14(4,11)	80.35	-5.3743	9.5	II .	ıı	
103356.6800(10)	14(5,10) - 14(-3,11)	80.35	-6.0910	1.8	"	ıı	
104077.7400(10)	14(4,10) - 14(4,11) + -	80.06	-6.0455	2.0	77.5	8.2	
104077.7500(10)	14(4,10) - 14(3,11) + -	80.06	-5.3703	9.4	"	II .	
104078.1700(10)	14(5,10) - 14(4,11) + -	80.06	-5.3703	9.4	"	"	
104078.1900(10)	14(5,10) - 14(3,11) + -	80.06	-6.0455	2.0	"	"	
104078.5800(10)	24(14,11) - 24(13,12) - +	266.33	-5.1099	29.0	"	"	
104574.9600(10)	13(3,10) - 13(*,11) - +	66.21	-5.3636	8.8	92.2	5.9	
104575.0300(10)	13(4,10) - 13(*,11) - +	66.21	-5.3636	8.8	"	"	
107339.7000(10)	22(12,11) - 22(11,12) - +	220.54	-5.1055	24.5	69.8	4.0	
107353.9100(10)	22(12,11) - 22(11,12)	220.55	-5.1025	24.7	98.8	11.9	
108601.4600(10)	21(-10,11) - 21(-9,12)	199.07	-5.1076	22.5	90.1	82.6	
108621.1100(10)	21(10,11) - 21(9,12) + -	199.03	-5.1107	22.3	96.2	43.9	

Table 8 continued on next page

Table 8 (continued)

Rest Frequency	Transition	$E_u$	$\log_{10} \frac{A_{ul}}{s^{-1}}$	$S_{ij}\mu^2$	P Factor	D Factor	Obs Ref
(MHz)		(K)		$(\text{Debye}^2)$	(%)	(%)	
108709.3300(10)	21(11,11) - 21(10,12)	199.08	-5.1065	22.5	88.2	1.3	
108797.3900(10)	21(11,11) - 21(10,12) + -	199.04	-5.1086	22.3	76.9	6.8	
108912.9900(10)	5(5,1) - 4(4,1)	15.80	-4.9257	8.7	75.7	27.9	
109835.4100(10)	20(-9,11) - 20(9,12)	178.54	-5.8830	3.5	59.3	1.6	
109837.5600(10)	20(-9,11) - 20(-8,12)	178.54	-5.1158	20.4	"	"	
109873.5600(10)	20(10,11) - 20(9,12)	178.54	-5.1154	20.4	94.2	0.5	
109875.7100(10)	20(10,11) - 20(-8,12)	178.54	-5.8826	3.5	"	"	
110079.5700(10)	20(10,11) - 20(9,12) - +	178.47	-5.1168	20.2	95.3	4.2	
110145.1600(10)	8(-2,6) - 7(3,5)	27.47	-4.9909	11.2	92.7	4.1	
110179.7400(10)	5(5,1) - 4(4,0) + +	15.62	-4.9042	8.8	75.8	6.7	
110358.1900(10)	8(2,6) - 7(3,5) + +	27.04	-4.9951	11.0	88.8	5.1	
110393.5000(10)	5(-5,0) - 4(-4,0)	16.20	-4.9056	8.7	64.7	9.8	
110499.9800(10)	8(3,6) - 7(2,5) + +	27.04	-4.9934	11.0	88.6	81.4	
110817.2500(10)	9(-1,8) - 8(2,7)	29.72	-4.8768	15.9	73.4	40.0	
110817.2800(10)	9(2,8) - 8(2,7)	29.72	-5.3410	5.5	"	ıı	
110817.5000(10)	9(-1,8) - 8(-1,7)	29.72	-5.3410	5.5	"	ıı	
110817.5400(10)	9(2,8) - 8(-1,7)	29.72	-4.8768	15.9	"	ıı	
110954.1100(10)	9(1,8) - 8(2,7)	29.27	-4.8820	15.7	99.0	39.3	
110954.1700(10)	9(2,8) - 8(2,7)	29.27	-5.3223	5.7	"	"	
110954.5500(10)	9(1,8) - 8(1,7)	29.27	-5.3223	5.7	"	"	
110954.6100(10)	9(2,8) - 8(1,7)	29.27	-4.8820	15.7	"	"	
111507.2800(10)	10(*,10) - 9(*,9)	31.02	-4.3757	54.8	99.4	86.7	(Remijan et al. 2003)
111548.5300(10)	10(*,10) - 9(*,9) + +	30.53	-4.3753	54.8	99.5	38.4	(Remijan et al. 2003)
112357.4100(10)	17(-6,11) - 17(6,12)	122.64	-5.9181	2.6	83.0	25.5	
112357.4400(10)	17(-6,11) - 17(-5,12)	122.64	-5.1808	14.0	"	"	
112358.1900(10)	17(7,11) - 17(6,12)	122.64	-5.1808	14.0	"	"	
112358.2200(10)	17(7,11) - 17(-5,12)	122.64	-5.9181	2.6	"	"	
112917.6300(10)	16(-5,11) - 16(*,12)	105.92	-5.1475	14.0	86.4	19.8	
112917.8000(10)	16(6,11) - 16(*,12)	105.92	-5.1475	14.0	II.	"	
112925.8100(10)	17(6,11) - 17(6,12) + -	122.46	-5.8710	2.8	99.6	9.4	
112925.8700(10)	17(6,11) - 17(5,12) + -	122.46	-5.1802	13.8	"	II.	
112927.3800(10)	17(7,11) - 17(6,12) + -	122.46	-5.1802	13.8	"	"	

Table 8 continued on next page

# Table 8 (continued)

Rest Frequency	Transition	$E_u$	$\log_{10} \frac{A_{ul}}{\mathrm{s}^{-1}}$	$S_{ij}\mu^2$	P Factor	D Factor	Obs Ref
(MHz)		(K)		$(\text{Debye}^2)$	(%)	(%)	
112927.4400(10)	17(7,11) - 17(5,12) + -	122.46	-5.8710	2.8	11	"	
113374.0500(10)	15(-4,11) - 15(*,12)	90.17	-5.2031	11.4	96.8	2.9	
113374.0800(10)	15(5,11) - 15(*,12)	90.17	-5.2031	11.4	"	"	
113600.7200(10)	16(5,11) - 16(5,12) - +	105.69	-5.8990	2.4	96.0	8.8	
113600.7300(10)	16(5,11) - 16(4,12) - +	105.69	-5.2201	11.7	"	"	
113601.0800(10)	16(6,11) - 16(5,12) - +	105.69	-5.2201	11.7	"	"	
113601.0900(10)	16(6,11) - 16(4,12) - +	105.69	-5.8990	2.4	"	"	
113742.2700(20)	14(*,11) - 14(*,12)	75.38	-4.9837	17.6	99.0	3.1	
114166.3000(10)	15(4,11) - 15(*,12) + -	89.89	-5.1921	11.5	96.1	8.0	
114166.3700(10)	15(5,11) - 15(*,12) + -	89.89	-5.1921	11.5	"	"	

Note—Pertinent parameters of the detected transitions of AcA taken from SLAIM catalog. The transitions with ditto marks in the column of P and D factors are blended with the transitions in the previous row.

### REFERENCES

- Balucani, N., Ceccarelli, C., & Taquet, V. 2015, MNRAS, 449, L16
- Belloche, A., Garrod, R. T., Müller, H. S. P., & Menten, K. M. 2014, Science, 345, 1584
- Belloche, A., Menten, K. M., Comito, C., Müller, H. S. P., Schilke, P., Ott, J., Thorwirth, S. & Hieret, C. 2008, A&A, 482, 179
- Belloche, A., Müller, H. S. P., Garrod, R. T. & Menten, K. M. 2016, A&A, 587, A91
- Belloche, A., Müller, H. S. P., Menten, K. M.; Schilke, P. & Comito, C. 2013, A&A, 559, 47
- Beltrán, M. T., Codella, C., Viti, S., Neri, R., & Cesaroni, R. 2009, ApJL, 690, L93
- Bennett, C. J., & Kaiser, R. I. 2007, ApJ, 660, 1289
- Bisschop, S. E., Jørgensen, J. K., van Dishoeck, E. F., & de Wachter, E. B. M. 2007, A&A, 465, 913

- Bonfand, M., Belloche, A., Menten, K. M., Garrod, R.T. & Müller, H. S. P. 2017, A&A, 604, A60
- Brouillet, N., Despois, D., Baudry, A., et al. 2013, A&A, 550, A46
- Brouillet, N., Despois, D., Lu, X.-H., et al. 2015, A&A, 576, A129
- Brown, R. D., Crofts, J. G., Godfrey, P. D., Gardner, F. F., Robinson, B. J. & Whiteoak, J. B. 1975, ApJ, 197, 29
- Burke, D. J., Puletti, F., Brown, W. A., et al. 2015, MNRAS, 447, 1444
- Butler, R. A. H., De Lucia, F. C., Petkie, D. T., Doug T., Møllendal, H., Horn, A. & Herbst, E. 2001, ApJS, 134, 319
- Calcutt, H., Viti, S., Codella, C., et al. 2014, MNRAS, 443, 3157

- Carroll, P. B., Drouin, B. J., & Widicus Weaver, S. L. 2010, ApJ, 723, 845
- Carroll, P. B., McGuire, B. A., Blake, G. A., et al. 2015, ApJ, 799, 15
- Carvajal, M., Willaert, F., Demaison, J., & Kleiner, I. 2007, Journal of Molecular Spectroscopy, 246, 158
- Chuang, K.-J., Fedoseev, G., Ioppolo, S., van Dishoeck, E. F., & Linnartz, H. 2016, MNRAS, 455, 170
- Condon, J. J. & Ransom, S. M. 2016, Essential Radio Astronomy (2nd ed.; Princeton: Princeton Univ. Press)
- Demyk, K., Wlodarczak, G., & Carvajal, M. 2008, A&A, 489, 589
- Garrod, R. T., & Herbst, E. 2006, A&A, 457, 927
- Garrod, R. T., Widicus Weaver, S. L., & Herbst, E. 2008, ApJ, 682, 283
- Graninger, D., Öberg, K. I., Qi, C., & Kastner, J. 2015, ApJL, 807, L15
- Halfen, D. T., Apponi, A. J., Woolf, N., Polt, R. & Ziurys, L. M. 2006, ApJ, 639, 237
- Halfen, D. T., Ilyushin, V. V., & Ziurys, L. M. 2015, ApJL, 812, L5
- Herbst, E., & van Dishoeck, E. F. 2009, ARA&A, 47, 427
- Hollis, J. M., Jewell, P. R., Lovas, F. J. & Remijan, A. 2004, ApJ, 613, 45
- Hollis, J. M., Jewell, P. R., Lovas, F. J., Remijan, A.,& Møllendal, H. 2004, ApJL, 610, L21
- Hollis, J. M., Lovas, F. J. & Jewell, P. R. 2000, ApJ, 540, L107
- Hollis, J. M., Vogel, S. N., Snyder, L. E., Jewell, P. R. & Lovas, F. J. 2001, ApJ, 554, 81

- Ilyushin, V. V., Alekseev, E. A., Dyubko, S. F.,
  Podnos, S. V., Kleiner, I. Margulès, L., Wlodarczak,
  G., Demaison, J., Cosléou, J., Maté, B., Karyakin,
  E. N., Golubiatnikov, G. Yu., Fraser, G. T.,
  Suenram, R. D., & Hougen J. T. 2001, Journal of
  Molecular Spectroscopy, 205, 286
- Ilyushin, V. V., Endres, C. P., Lewen, F., Schlemmer, S., & Drouin, B. J. 2013, Journal of Molecular Spectroscopy, 290, 31
- Karton, A.& Talbi, D. 2014, Chemical Physics, 436, 22
- Kobayashi, K., Ogata, K., Tsunekawa, S., & Takano, S. 2007, ApJL, 657, L17
- Laas, J. C., Garrod, R. T., Herbst, E., & Widicus Weaver, S. L. 2011, ApJ, 728, 71
- Lattelais, M., Bertin, M., Mokrane, H., et al. 2011, A&A, 532, A12
- Lattelais, M., Pauzat, F., Ellinger, Y., & Ceccarelli, C. 2009, ApJL, 696, L133
- Lattelais, M., Pauzat, F., Ellinger, Y., & Ceccarelli, C. 2010, A&A, 519, A30
- Linnartz, H., Ioppolo, S., & Fedoseev, G. 2015, Int. Rev. Phys. Chem. 34, 205
- Liu, S.-Y., Girart, J. M., Remijan, A. J., & Snyder, L.E. 2002, ApJ, 576, 255
- Liu, S.-Y., Mehringer, D. M., & Snyder, L. E. 2001, ApJ, 552, 654
- Loomis, R. A., McGuire, B. A., Shingledecker, C., Johnson, C. H., Blair, S., Robertson, A. & Remijan, A. J. 2015, ApJ, 799, 34
- Mangum, J. G., & Shirley, Y. L. 2015, PASP, 127, 266
- McGuire, B. A., Carroll, P. B., Loomis, R. A., et al. 2016, Science, 352, 1449

KUE ET AL.

- McGuire, B. A., Shingledecker, C. N., Willis, E. R., Burkhardt, A. M., El-Abd, S., Motiyenko, R. A., Brogan, C. L., Hunter, T. R., Margulès, L., Guillemin, J.-C., Garrod, R. T., Herbst, E. & Remijan, A. J. 2017, ApJL, 851, L46
- McMullin, J. P., Waters, B., Schiebel, D., Young, W., & Golap, K. 2007, Astronomical Data Analysis Software and Systems XVI, 376, 127
- Mehringer, D. M., Snyder, L. E., Miao, Y. & Lovas, F. J. 1997, ApJ, 480, 71
- Mottlad, M. J., Glazerad, B. T., Kaiserbd, R. I. & Meechcd, K. J. 2007, ChEG 67, 253
- Müller, H. S. P., Schlöder, F., Stutzki, J., & Winnewisser, G. 2005, Journal of Molecular Structure, 742, 215
- Öberg, K. I., Bottinelli, S., Jørgensen, J. K., & van Dishoeck, E. F. 2010, ApJ, 716, 825
- Öberg, K. I., Guzmán, V. V., Furuya, K., Qi, C., Aikawa, Y., Andrews, S. M., Loomis, R. & Wilner, D. J. 2015, Nature, 520, 198
- Oesterling, L. C., Albert, S., De Lucia, F. C., Sastry, K. V. L. N., & Herbst, E. 1999, ApJ, 521, 255
- Ogata, K., Odashima, H., Takagi, K., & Tsunekawa, S. 2004, Journal of Molecular Spectroscopy, 225, 14
- Pickett, H. M., Poynter, R. L., Cohen, E. A., Delitsky,M. L., Pearson, J. C. & Muller, H. S. P. 1998, J.Quant. Spectrosc. & Rad. Transfer, 60, 883
- Puletti, F., Malloci, G., Mulas, G., & Cecchi-Pestellini, C. 2010, MNRAS, 402, 1667
- Qin, S.-L., Schilke, P., Rolffs, R., Comito, C., Lis, D.C. & Zhang, Q. 2011, A&A, 530, 9
- Remijan, A. J., Adams, M. & Warmels, R. 2015, ALMA Cycle 3 Technical Handbook Version 1.0, ALMA

- Remijan, A. J., Hollis, J. M., Lovas, F. J., Plusquellic,D. F. & Jewell, P. R. 2005, ApJ, 632, 333
- Remijan, A. J., Snyder, L. E., Friedel, D. N., Liu, S.-Y.
  & Shah, R. Y. 2003, ApJ, 590, 314
- Remijan, A. J., Snyder, L. E., McGuire, B. A., et al. 2014, ApJ, 783, 77
- Remijan, A., Snyder, L. E., Liu, S.-Y., Mehringer, D., & Kuan, Y.-J. 2002, ApJ, 576, 264
- Requena-Torres, M. A., Martín-Pintado, J., Rodríguez-Franco, A., et al. 2006, A&A, 455, 971
- Sakai, Y., Kobayashi, K., & Hirota, T. 2015, ApJ, 803, 97
- Sánchez-Monge, Á., Schilke, P., Schmiedeke, A., et al. 2017, A&A, 604, A6
- Shaw, R. A., Hill, F., & Bell, D. J. 2007, Astronomical Data Analysis Software and Systems XVI, 376,
- Skouteris, D., Balucani, N., Ceccarelli, C., et al. 2018, ApJ, 854, 135
- Snyder, L. E., Kuan, Y.-J., & Miao, Y 1994, in TheStructure and Content of Molecular Clouds, ed. T.L. Wilson & K. J. Johnson (Berlin: Springer), 87
- Snyder, L. E., Lovas, F. J., Hollis, J. M., Friedel, D. N., Jewell, P. R., Remijan, A., Ilyushin, V. V., Alekseev, E. A. & Dyubko, S. F. 2005, ApJ, 619, 914
- Townes, C. H., & Schawlow, A. L. 1975, Microwave Spectroscopy (New York: Dover)
- Turner, B. E. 1991, ApJS, 76, 617
- Wächtershaüser G., 2000, Science, 289, 1307
- Watanabe, N., & Kouchi, A. 2002, ApJL, 571, L173
- Widicus Weaver, S. L., Butler, R. A. H., Drouin, B. J., et al. 2005, ApJS, 158, 188
- Woods, P. M., Kelly, G., Viti, S., et al. 2012, ApJ, 750, 19